Properties of Rapidly Rotating Stars and Their Oscillation Modes

by

Diego Castañeda

A Thesis Submitted to Saint Mary's University, Halifax, Nova Scotia in Partial Fulfillment
of the Requirements for the Degree of PhD in Astronomy
(Department of Astronomy and Physics)

2016, Halifax, Nova Scotia

Approved: Dr. Robert Deupree

Advisor

Approved: Dr. David Guenther

Reader

Approved: Dr. Ian Short

Reader

Approved: Dr. Alison Sills

External Examiner

Date: June 2, 2016.

Acknowledgements

I would like to thank my supervisor, Dr. Robert Deupree for giving me the opportunity to work with him over the last five and a half years. His guidance, patience and wisdom helped me making this thesis happen. I would also like to thank Dr. David Guenther for adopting me as his graduate student for the last two years, always providing me with help and support whenever I needed.

This thesis required many hours of work and dedication that would have hard to accomplish if it was not for the continuous support of my family and friends. I also appreciate all the good times and discussions with my fellow graduate students at the Department of Astronomy and Physics. Finally, I want to give special thanks to Anneya and Rasalhague for always being there with me on this journey. I look forward to our next adventure.

Contents

List of Figures

List of Tables

Abstract

Properties of Rapidly Rotating Stars and their oscillation modes

by Diego Castañeda

In this thesis I present a set of scaling relationships for ZAMS rotating models. These relationships are applicable to models whose rotation rate produces a given surface distortion and are shown to be valid for stellar masses from 1.875 $M_{\odot}$ to 2.5 $M_{\odot}$. Some of the scaling relationships are used to determine intrinsic stellar properties such as the real luminosity and effective temperature of the star based on deduced properties from interferometry and other observations, providing a direct way to place a rotating star into the HR diagram. I also present pulsation calculations of p and g-modes for a set of these rotating models using a 2D linear adiabatic code. I computed and classified more than ten thousand pulsation modes and found scaling relationships for both the p-modes and g-modes between models of different masses with the same surface shape. The p-mode scaling is well-described by the root-mean density relation but the scaling of g-modes is found to depend on properties outside of the convective core. These pulsation mode scaling properties could be useful for selecting optimal stellar models to match the observed oscillation frequencies of individual stars. Finally, I considered the observability of the modeled oscillation modes by perturbing the surface properties of static rotating models and calculating the effect each mode would have on the observed magnitude of the star at different inclinations. The results suggest that there are some modes that could be ruled out from the analysis when comparing the theoretical and observed oscillation spectra of a rotating star for the rotation rates considered.

June 2, 2016

Chapter 1

Introduction

1.1 Background

The structure and evolution of non-rotating spherical stars has been well understood (this is not to say that there are no remaining issues) for a wide a range of masses and metallicities for all but the most advanced evolucionary states for a good part of the last 50 years. The basic equations that govern the stellar structure have been successful at reproducing the broad stellar properties observed in objects such as stellar clusters, which are often good test beds for stellar evolution studies. In its most basic form a static spherical star can be modeled as a 1D (spherically symmetric) object where the Lagrangian equations that describe its structure are the hydrostatic equilibrium relation

$$\frac{dP}{dm} = -\frac{Gm}{4\pi r^4}, \tag{1.1}$$

where P is the pressure, m is the mass interior to the radius, r, and G is the gravitational constant; the mass conservation equation,

$$\frac{\partial r}{\partial m} = \frac{1}{4\pi r^2 \rho}, \tag{1.2}$$

where ρ is the density; the energy conservation equation,

$$\frac{dL_r}{dm} = \epsilon, \tag{1.3}$$

where ϵ is the total energy released per unit mass per second by all nuclear reactions and L_r is the energy flow rate through a sphere of radius r. The energy transport equation, that can take different forms depending on the conditions inside of the star:

$$\begin{aligned} \tfrac{\partial \ln T}{\partial \ln P} &= \min(\nabla_{\rm rad}, \nabla_{\rm ad}), \\ \nabla_{\rm rad} &= \tfrac{3}{16\pi acG} \tfrac{\kappa P}{T^4} \tfrac{L_r}{m} \\ \nabla_{\rm ad} &= \tfrac{\Gamma_2 - 1}{\Gamma_2} \end{aligned} \tag{1.4}$$

where ∇ depends on the type of energy transport involved, $\nabla = \min(\nabla_{\rm rad}, \nabla_{\rm ad})$. The radiative gradient is used in convectively stable region and the adiabatic gradient for convectively unstable regions well below the surface of the model. The surface convection zones for the stars we will be considering are so inefficient that the radiative gradient is very close to the actual gradient and will be used.

Finally, the equation of state

$$P = P\,(\rho,\, T,\, \text{composition}) \tag{1.5}$$

and subsidiary relations for the opacity and nuclear energy generation complete the equations to be solved. Stars undergo several "stages" of burning material but they spend most of their lifetime fusing hydrogen into helium through a sequence of reactions called the proton-proton chain for stars with masses below about $1.5\mathrm{M}_{\odot}$ and the CNO cycle for stars with higher masses.

Several processes can affect the equilibrium assumed by these equations. Stars are not in perfect equilibrium, starting with the Sun that shows light variations all over its surface. Careful examination of stars through traditional observations such as photometry and spectroscopy all over the HR diagram have shown that many stars are far from being static and that many more show small amplitude variations about its static state. For example, stars situated on the classical Cepheid instability strip show periodic light variations that require linear perturbation or nonlinear hydrodynamic simulations in order in order to understand such behavior. While there remain a number of problems, the simulations of spherically symmetric stars have enjoyed a great degree of success in aiding our understanding of stellar structure, evolution, and pulsation.

However, not all stars can be considered spherically symmetric due to the presence of significant stellar rotation or magnetic fields (or possibly both). In this work we will consider only stellar rotation. Historically, stellar rotation was inferred mainly through

Doppler broadening of spectral lines, first predicted by Shajn & Struve (1929) and then applied by Elvey (1930), Struve & Elvey (1931), and Slettebak (1949) to show that most rapidly rotating stars were early type stars in general and A stars in particular, with the largest rotating velocities being 300 - 400 km s^{-1}.

Significant advances in the understanding of stellar interior and evolution of rapidly rotating stars have been limited by theoretical and observational complications. Rapidly rotating stars with sufficiently large centrifugal forces distort considerably the surface of the star. Rotation can also generate hydrodynamic and thermal instabilities in the interior of the star that may change its composition and rotation profiles and consequently affect the star's properties and evolution. Observationally, the properties of a sufficiently rapidly rotating star deduced from traditional observations are tightly related to the angle of inclination with respect to the rotation axis at which the observations are made. Because of this, deducing the location of rotating stars in the HR diagram, their masses, lifetimes and other deduced parameters derived from the assumption of spherical symmetry need to be revised.

The combination of optical interferometry and asteroseismology of rapidly rotating stars has been recognized within the past decade as a key step towards a better understanding of the effects that rotation has in the internal structure and evolution of stars (Cunha et al. 2007). While asteroseismology depends strongly on the availability of accurate global stellar parameters which are not usually directly observable for rotating stars, interferometry can provide both the otherwise unknown oblateness (which provides some estimate of the strength of the rotation) and inclination of the rotation axis to the observer. Interferometry has been successfully applied to a number of rapid rotators (van Belle et al. 2001; Domiciano de Souza et al. 2003; Aufdenberg et al. 2006; Monnier et al. 2007; Zhao et al. 2009; Che et al. 2011; Hadjara et al. 2014). Still, the agreement between observation and theory is far from complete and significant advances have been limited.

Numerous observations of stellar oscillation frequencies from space based missions such as MOST (Walker et al. 2003), CoRoT (Baglin et al. 2009), and Kepler (Basri et al. 2005) are generating a large number of oscillation frequencies for a large number of stars. For those stars which are rotating, the oscillation frequencies depend on the rotational properties of the star and successful matching of these frequencies could lead to a better understanding of rotation and its effects in stars. It is of great importance to obtain ways to find the intrinsic properties in rapidly rotating stars if we want to take full advantage of observational techniques such as asteroseismology, where appropriate modeling of the oscillation frequencies requires the internal structure to be as realistic as possible. The next sections present some of the theory required to study stellar rotation and finally discuss the objectives of this thesis.

1.1.1 Modeling Rotating Stars

To model a rotating star, the four equations of stellar structure need to be modified and a new equation, Poisson's equation for the gravitational potential, introduced. Although the same physics is applied, the problem is no longer spherically symmetric and should be solved in two dimensions (assuming the rotating model is a spheroid) to realistically account for all the effects introduced by rotation.

Initially, rotational effects were treated as a first order perturbation to one dimensional models. For example, Sweet & Roy (1953) calculated first order perturbations to produce a rotating Cowling model. This particular approach gave some useful answers for slowly rotating models, but breaks down for moderately rotating models. Monaghan & Roxburgh (1965) developed a method to simulate the structure or rotating stars using polytropes. The method has been used and extended to more realistic models by others (e.g., Roxburgh et al. 1965; Faulkner et al. 1968; Kippenhahn & Thomas 1970; Sackmann & Anand 1970) and by Endal & Sofia (1976; 1978) to include the redistribution of angular momentum in this 1D framework for a number of hydrodynamic and thermal instabilities.

One of the most famous approximations used to compute rotating models still used today is known as von Zeipel (1924) theorem. He found that for uniformly rotating models the state properties remained constant on equipotential surfaces when radiative equilibrium was assumed. This means that the surface flux is proportional to the local gravity. Applying the Stefan-Boltzmann law, von Zeipel's law implies that $T_{\rm eff} \propto g^{0.25}$.

Knowing that the state variables are constant on equipotential surfaces led to the development of two computational approaches for calculating rotating stellar models. One of them, the self-consistent field method (Ostriker & Mark 1968), was used to solve for the gravitational potential given density distribution and then solved for a new density distribution on equipotential surfaces from hydrostatic equilibrium. Using the new gravitational potential, the process can be iterated until all changes are sufficiently small. Jackson (1970) and more recently Jackson et al. (2005) and MacGregor et al. (2007), extended the method of solution to include all equations of stellar structure.

For this thesis we use models generated by the 2.5D stellar structure and evolution code, ROTORC (Deupree, 1990; 1995). The models are a subset of the suite of ZAMS models generated by Deupree (2011a) and only include masses between $1.875\mathrm{M}_\odot$ and $3\mathrm{M}_\odot$. ROTORC computes models on a 2D finite-difference grid whose independent variables are the fractional surface equatorial radius (x) and the colatitude (θ). For ZAMS models a rotation rate is imposed as a function of x and θ in terms of the azimuthal velocity, v_ϕ. These particular models assume a solid body rotation law and their composition is taken to be $\mathrm{X} = 0.7$, $\mathrm{Z} = 0.02$. The equations solved by ROTORC to generate these models are the time-independent equations of hydrostatic and thermal equilibrium, Poisson's equation, the equation of state, and relations for the nuclear energy generation and the radiative opacity. These equations are solved simultaneously for the density, pressure, temperature, and gravitational potential at each location in the 2D grid using the Henyey technique.

Boundary conditions are imposed at the surface of each model. The density is set to some very small value and the surface temperature is set equal to the effective temperature divided by the fourth root of two. The temperature relation comes from applying an Eddington atmosphere

$$T^4(\tau) = \frac{3}{4} T_{\mathrm{eff}}^4 (\tau + 2/3) \tag{1.6}$$

at $\tau = 0$. This relationship between the effective temperature and the local temperature is contradictory to von Zeipel's law, which forces the temperature to be constant on an equipotential surface (including the stellar surface), even though the effective temperature can vary by a significant factor between the pole and equator. Recent studies have also shown that the gravity darkening observed in rotating stars without substantial surface convection zones is not best represented by von Zeipel's law but rather a more general relation of T_{eff} proportional to g_{eff}^{β} (Lovekin et al. 2006; Zhao et al. 2009; Espinosa Lara & Rieutord 2011; Claret 2012). The application of this relation using β as a free parameter in interferometric studies show that $\beta = 0.25$ seems to overestimate the temperature difference between pole and equator, requiring a β value closer to 0.2 (Monnier et al. 2007; Zhao et al. 2009; Che et al. 2011; Claret 2016) which is close to what ROTORC models produce.

1.1.2 Properties and SED calculation of δ Scuti stars

Promising candidates for testing our theoretical undestanding of rotation and and asteroseismology are δ Scuti stars. These variables are Population I stars positioned at an extension of the classical Cepheid instability strip down to where it crosses the main sequence in the HR diagram. Typical spectral classes range approximately from A to early F with luminosity classes V to III. Their pulsation amplitudes range from tenths of magnitudes down to the millimagnitude level. The largest amplitude δ Scuti stars are known as high-amplitude δ Scuti stars (HADS). Pulsation frequencies for these stars typically range from 5 to 80 cycles/day and the pulsation modes may be radial or non-radial in nature. These pulsators are also often found to be rapidly rotating, which can complicate their oscillation spectra significantly.

Rapidly rotating stars are sufficiently oblate that their emergent spectral energy distribution (SED) depends on the stellar latitude, so that an observer will make different determinations of such basic properties as the luminosity and effective temperature depending on the inclination of the rotation axis to the observer. If the star rotates as a solid body, the values of the effective temperature (T_{eff}) and the effective gravity (g_{eff}) at the pole are larger than at the equator, making the star both hotter and brighter when viewed pole-on than when viewed equator on. This effect makes the determination of intrinsic properties such as the star's actual luminosity L and actual T_{eff} quite difficult. The effect can be quite pronounced at sufficiently large rotation - a star's classification can vary three or more subtypes (Slettebak et al. 1980; Collins & Smith 1985; Gillich et al. 2008). An uncertainty this large in the placement of a star in the HR diagram makes the matching of observed and computed oscillation mode frequencies more complex because it vastly increases the number of models that have to be considered. A mechanism is required to more reasonably determine the properties of an observed rotating star.

It is possible to use the surface properties of structure models like those calculated with ROTORC to construct a simulated SED of a rotating star at various inclinations. This is done by integration over the visible surface of the star seen from some inclination using the intensities emerging from atmosphere models defined by the local surface parameters of the star.

Model atmospheres will produce the intensity emerging from the atmosphere as a function of the direction with respect to the local surface normal. Taking the component of each set of rays in the direction of the observer, it is possible to determine the flux at each wavelength that will be observed at some distance from the star. The general expression for this integration in spherical coordinates would be:

$$F_\lambda(i) = \int_\theta \int_\phi I_{\lambda'}(\psi(\theta, \phi, i)) W(\lambda, \lambda') \frac{\mathrm{d}A_{\mathrm{proj}} \cos\psi(\theta, \phi, i)}{d^2} \tag{1.7}$$

where ψ is the angle between the local normal and the direction to the observer. $W(\lambda, \lambda')$ denotes the wavelength change produced by the Doppler shift. The area element of projected area, $\mathrm{d}A_{\mathrm{proj}}$, is given by

$$\mathrm{d}A_{\mathrm{proj}} = R^2(\theta) \sin\theta \cos\psi \sqrt{1 + \left(\frac{\mathrm{d}R}{\mathrm{d}\theta}\right)^2 \frac{1}{R^2}} \mathrm{d}\theta \mathrm{d}\phi \tag{1.8}$$

This method has been applied by several other studies to obtain SEDs for non-spherical stars (e.g., Slettebak et al. 1980; Linnell & Hubeny 1994; Frémat et al. 2005; Lovekin et al. 2006; Gillich et al. 2008).

For this work we used the model atmospheres calculated by PHOENIX version 15 (Hauschildt & Baron 1999). The PHOENIX atmospheres used include non-LTE effects as outlined by Short et al. (1999) to allow at least two ionization stages of 24 elements and the lowest six ionization stages of the 20 most important elements, including several of the Fe group elements.

The observed luminosity and photometric colors can be calculated from this SED. All of these quantities will clearly depend on the inclination angle so there will be simulated observed quantities for each inclination angle considered. In the past this has limited the determination of the intrinsic properties of stars undergoing rotation because there is no straightforward way of determining the inclination angle at which the star is observed. But advances in optical interferometry instrumentation can provide the determination or constraint of this parameter. As mentioned previously, interferometry has successfully resolved a small number of stars, opening the door to greater advances in modeling of stellar rotation.

It is important to note, however, that the determination of the intrinsic properties using realistic models is still a fairly complex process that requires several steps and relatively large computational resources. Fortunately, there are certain scaling relationships relating the latitudinal variation of the effective temperature and surface radius, along with the actual luminosity and effective temperature (the latter determined from the actual luminosity and the effective radius, which is defined as the radius of a sphere which has the same surface area as the oblate spheroid) between two different models which have some similar properties. The generation of these scaling relationships is the subject of the second chapter of this thesis. The existence of these scaling relationships means that having a model relatively close to matching the observed SED can be perturbed by small changes in the mass and surface radius scale (keeping the oblateness the same) to produce a model with the correct properties.

In general large amplitude pulsation can be understood as (most often) a standing wave associated with a particular oscillation mode that due to the internal configuration of the star grow to have amplitudes sufficiently large to change the star considerably through one pulsation cycle. In the case of δ Scuti stars the pulsations are driven by a mechanism known as the κ, or opacity, mechanism in the hydrogen and helium ionization regions. When the material in these ionization zones is compressed the density and temperature as well as the opacity increases, trapping some of the radiation and causing pressure to accumulate in the interior layers of the star. Eventually the pressure will be enough to push the outer layers outward and the ionization regions delay the time of peak pressure until after the time of maximum contraction, so that the pressure gradient is pushing the star out while it is moving out. Finally, during the expansion the ionization layers will cool and the opacity will decrease, allowing the trapped energy to be radiated and the pressure inside beneath the ionization layer will decrease, forcing the star to contract. The cycle will repeat as long as the conditions are appropriate.

1.1.3 Computing Linear, Adiabatic, Nonradial Oscillation Frequencies

The simplest method to compute the oscillation mode frequencies is to solve the appropriate linear, adiabatic perturbations of equations of momentum, mass, the adiabatic relation between density and pressure, and Poisson's equation for the gravitational potential

$$\sigma^2 \rho \overrightarrow{\xi} + 2i\sigma(\overrightarrow{\xi} \times \overrightarrow{\Omega}) + \overrightarrow{g}\delta\rho - \overrightarrow{\nabla}\delta P + \rho\overrightarrow{\nabla}\delta\Phi = 0 \tag{1.9}$$

$$\delta\rho = -\overrightarrow{\nabla} \cdot \rho \overrightarrow{\xi} \tag{1.10}$$

$$\delta P = -\Gamma_1 P \overrightarrow{\nabla} \cdot \overrightarrow{\xi} - \overrightarrow{\xi} \cdot \overrightarrow{\nabla} P \tag{1.11}$$

$$\nabla^2 \delta\Phi = -4\pi G \delta\rho, \tag{1.12}$$

where $\overrightarrow{\xi} = \xi(\xi_r, \xi_\theta, \xi_\phi)$ is the Lagrangian perturbation of the location, δP and $\delta\rho$ are the linear (Eulerian) perturbations to the pressure and density respectively. $\delta\Phi$ denotes the linear perturbation of the gravitational potential. Finally, $\overrightarrow{g}$ is the effective gravity. For non-rotating cases, all the coefficients of the perturbations are spherically symmetric which means that the only the non-spherical components will be the perturbations themselves, allowing radial and angular perturbations to have the form

$$\xi_r(r,\theta) = A\,Y_\ell^m(\cos\theta) \tag{1.13}$$

$$\xi_\theta(r,\theta) = B\frac{dY_\ell^m(\cos\theta)}{d\theta} \tag{1.14}$$

where A and B are functions only of r. The pressure and density perturbations are 180 degrees out of phase with ξ_r and have the same Y_m^ℓ dependence.

Each oscillation frequency and eigenfunction is defined by three quantum numbers: n, ℓ, and m. Each number provides a characteristic of the pulsation mode: n is generally the number of radial nodes of the mode, ℓ is the number of latitudinal nodes and is also known as the "harmonic degree", and m represents the number of meridional nodes and is confined to values of $-\ell \leq m \leq \ell$. Radial only modes are denoted by $\ell = 0$, where the mode with $n = 0$ is known as the fundamental mode, followed by the first overtone ($n = 1$, also known as 1H), and so on for higher n values. Modes can also be sub-classified based on their two main restoring forces: pressure modes (p modes) where, as its name suggests, the pressure serves as the restoring force and gravity modes (g modes) where gravity is the restoring force. Low order pressure modes probe the bulk of the star and higher n p modes effectively probe the layers between the surface and the location of the radial node closest to the surface, while the g modes are more sensitive to the properties just outside the convective core for the δ Scuti models we will be considering.

Some processes such as evolution or rotation can change the stellar structure in such a way that the frequencies of some modes of the same harmonic parity approach each other in frequency space causing the properties of each mode to be altered by the other. These mode interactions are also known as “avoided crossings”. Frequency regions where g modes and p modes overlap often present challenges for their classification because of the number of alterations that can occur. Evolution and processes like rotation can cause modes in these frequency regions to show a “mixed” behavior because they display characteristics of p modes in the outer parts of the star and g modes characteristics in the interior outside the convective core. Appropriately, they are often referred as “mixed modes” and they are an interesting case of study in stellar pulsation because their dual properties may allow a mode that is excited near the core to show large enough amplitudes in the p mode region, potentially allowing its detection on an observed oscillation spectra.

An important concept regarding the g modes that will also be used in this thesis is the Brunt-Väisälä frequency N, which is also known as the buoyancy frequency and is defined as

$$N^2 = g\left(\frac{1}{\Gamma_1}\frac{\mathrm{d}\ln p}{\mathrm{d}r} - \frac{\mathrm{d}\ln \rho}{\mathrm{d}r}\right). \tag{1.15}$$

For a blob of fluid perturbed on layer stratified under gravity, values of N^2 larger than zero indicate that the blob is heavier than the displaced fluid and buoyancy should force it back towards its original position, the blob will then oscillate around an equilibrium position. On the other hand if $N^2 < 0$, the blob is lighter than the fluid it displaces and buoyancy will only enhance its motion pushing it further away from equilibrium.

The asteroseismic picture is complicated further if the star is no longer spherically symmetric, as is the case for rotating stars. Special considerations are required in order to account for this effects and are addressed in the following section.

1.1.4 Asteroseismology of rotating stars

Most initial attempts to model pulsation mode frequencies in rapidly rotating stars assume that rotation can be included into the models as a perturbation and that it is much smaller than the frequencies calculated. This allows the rotation to be included as a power series in the rotation rate. The series has been studied to first (Ledoux 1949; Cowling & Newing 1949), second (Simon 1969; Saio 1981) and third order (Soufi et al. 1998). For nonrotating models, the modes for a given n and ℓ have the same frequency for all values of m, and the first order perturbations lift this degeneracy. The second order perturbations change all frequencies. Lovekin et al. (2009) showed that the rotation rate does not have to be very large before the results of the perturbation approach differ from those of more realistic treatments.

As discussed in the first section rotation causes the spherical symmetry in the star to be lost and the linearized equations shown in the previous section are no longer separable in r and θ. This makes the problem considerably harder to solve. A general mathematical treatment to address this is to express the perturbations a summation of spherical harmonics (Lee & Saio 1986).

Efforts to more accurately include rotation have been developed but these methods require multidimensional calculations that are often more time consuming and complex to perform. Some efforts to simplify the problem have been made. Espinosa et al. (2004) calculated the adiabatic oscillations of rapidly rotating stars with uniform rotation by applying the the Cowling approximation and neglecting both the Coriolis force and the Brunt-Vaisala frequency in the adiabatic equation. Other studies modelled quasi-radial modes at a range of rotation rates in rotating neutron stars using the relativistic Cowling approximation (Yoshida & Eriguchi 2001). Lignières et al. (2006) and Reese et al. (2008) included fewer physical restrictions but their models were restricted polytropic representations. More recently, Ouazzani et al. (2012) and Ouazzani et al. (2015) used a method introduced by Roxburgh (2006) and based on the self consistent method to produce more realistic 2D rotating models. From these models they calculated linear adiabatic oscillation modes using a spectral method. Lignières & Georgeot (2009), and Pasek et al. (2012) and used a ray tracing technique to study the acoustic properties of rapidly rotating polytropes. The study found that for high rotational velocities three different groups of modes could be found: island modes, corresponding to small $\ell - |m|$ in the non-rotating case; whispering gallery modes, corresponding to large $\ell - |m|$ values; and chaotic modes, corresponding to intermediate $\ell - |m|$ values in the non-rotating case.

For this work we use the 2D linear adiabatic pulsation code NRO developed by Clement (1998). This code uses the 2D stellar structure of models produced by ROTORC and solves the linearized non-radial pulsation equations on a selected number of radial line of a 2D grid. NRO performes a series of variable transformations to solve for the eigenfunctions in terms of the traditional variables show in equations 1.9 to 1.12:

$$\begin{aligned}
y_1 &= \tfrac{\xi_r}{r^{|k-1|}\sin^m\theta}, \\
y_2 &= \tfrac{\xi_\theta}{r^{|k-1|}}\sin^{|m-1|}\theta\cos\theta, \\
y_3 &= \tfrac{\delta p}{r^k\sin^m\theta}, \qquad (1.16) \\
y_4 &= \tfrac{\delta\phi}{r^k\sin^m\theta}, \\
y_5 &= \partial_r y_4,
\end{aligned}$$

where the value of k is related to the way that the pressure perturbation is expressed as a function of radial components:

$$\delta P(r,\theta,\phi;n,\ell,m) = e^{im\phi}\sum_{k=m}^{\infty} A_k^m(r,\theta;n,\ell)\,r^k. \qquad (1.17)$$

The code finds solutions for a range of k values performing finite difference integrations in N radial directions, where N is also the number of associated Legendre polynomials used to describe the latitudinal variation (also known as basis functions). It does one integration for each member of the basis function set at each of the N evenly spaced latitudinal locations.

Linear adiabatic solutions like the ones produced by NRO provide reasonable oscillation frequencies (at least for delta Scuti stars), but they do not contain any information about the thermal processes inducing the pulsations inside of the star. Thus, the adiabatic approach provides no information about the stability of the individual pulsation modes. The only way to obtain this information in the linear regime is by performing non-adiabatic calculations which are more difficult to solve and require dealing with complex variables. Work to include non-adiabatic effects into pulsation calculations for 1D non-rotating models have been sucessfully done in the past (Saio & Cox 1980; Pesnell 1990; Guenther 1994; Dupret et al. 2002; Suran 2008) but results for linear, nonadiabatic, nonradial calculations of rotating stars are not yet available.

Assuming that a calculated model can be used to study the oscillation frequency spectrum observed from a rotating star such as a δ Scuti star, it is unlikely that the computed mode frequencies will be a match to the observed ones. In some cases the model can be changed to bring the observed and computed frequencies into close agreement but as has been shown, the process of model generation and mode calculation can be quite complex. It would be ideal to find similar relationships between pulsation frequencies as the one that exist for non-rotating model p modes, known as the period-mean density relation. The subject of the third chapter of this thesis is looking for such relationships for rotating stars, both for the p modes and the g modes.

1.1.5 Mode observability

A particular example of a promising rapid rotator that has been observed interferometrically (Zhao et al. 2009) as well as asteroseismologically with MOST (Monnier et al. 2010) is α Oph (Rasalhague). Rotating at an estimated equatorial velocity (V_{eq}) of 240 km s^{-1}, MOST observations reportedly found 57 oscillation frequencies that include both p and g modes. With this information, Deupree et al. (2012) attempted to match simultaneously the observed spectral energy distribution, V_{eq}, and the observed oblateness and some of the highest amplitude modes, excluding the low frequency g modes, determined with the MOST data. The computed SED provided a good match to the observed one but a less

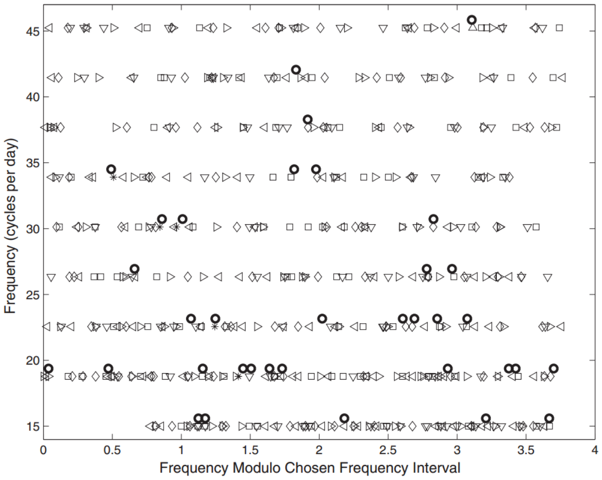

Figure 1.1: Echelle diagram of the α Oph observed oscillation frequencies (circles) and the calculated frequencies. The observed frequencies are slightly vertically offset from the calculated ones. The different symbols represent the different values of $\mid m \mid$=0, 1, 2, 3, 4. Taken from Deupree et al. 2012.

ideal situation was found matching the modes observed. Figure 1 shows the echelle diagram of the observed oscillation frequencies and the calculated frequencies, and it highlights one of the biggest problems that is found matching observed frequencies with the linear codes available. The frequency space of the calculated modes is so dense that it is difficult to point to any successful match as resulting from other than chance.

The photometric determination of mode frequencies also produces the amplitudes of the individual modes, and it generally argued that one feature determining the mode amplitude is the effect of cancellation. This is due to the fact that we observe only the averaging of brighter and darker areas on the surface of distant stars. It is often claimed that it is only possible to observe pulsation modes with $\ell \leq 3$ (Dziembowski 1977) for nonrotating stars, due to cancellation effects, allowing the omission of any higher harmonic degree modes at the time of comparison with observations. This is not so clear for rapidly rotating stars, where modes can be strongly changed by rotation and require that the latitudinal variation be expressed as a sum of Legendre polynomials, so the criterion for omitting modes based on observability needs to be investigated further. This is done in the fourth chapter of this thesis.

Finally, we present a few brief comments on the totality of our work in the final chapter.

Chapter 2

Scaling of Observable Properties in Rotating Stars

The contents of this chapter originally appeared as Castañeda, D. and Deupree, R. G. 2014, The Astrophysical Journal , 794, 13. They are reproduced here in accordance with the copyright policy outlined by the publisher (https://aas.org/publications/aas-copyright-policy).

The spectral energy distribution as a function of inclination is computed using 2D rotating stellar models and NLTE plane parallel stellar atmospheres. These models cover the range from $1.875 M_\odot$ to $3.0 M_\odot$. The deduced effective temperature is determined by B-V computed from the spectral energy distribution, and the deduced luminosity is computed as the integral of the spectral energy distribution over all frequencies, assuming the distance and reddening are known. These deduced quantities are obtained from the observed spectral energy distribution assuming the objects are spherically symmetric, and thus the results are dependent on the inclination. Previous work has shown that the surface properties between two rotating stellar models with the same surface shape scale, and this is also true for the deduced effective temperature and luminosity over this limited mass range.

2.1 INTRODUCTION

Advances in the general study of rotating stars have been limited by both theoretical and observational difficulties. A key example is that fundamental properties such as the effective temperature (T_{eff}) and luminosity (L) that one would deduce from observations now depend significantly on the angle of inclination (i) between the line of sight and the star's rotation axis for sufficiently rapidly rotating stars (e.g., Collins & Harrington 1966; Hardorp & Strittmatter 1968; Maeder & Peytremann 1970). This greatly complicates the determination of the star's position on the HR diagram and hence nearly all other useful information unless its inclination can be determined.

Given a grid of plane parallel model atmospheres and a rotating model with latitudinal variation in the surface effective temperature and effective gravity, one can compute the spectral energy distributions (SED) for any inclination by performing a weighted integral of the intensity in the direction of the observer over the visible surface of the star (e.g., Slettebak et al. 1980; Linnell & Hubeny 1994; Frémat et al. 2005; Lovekin et al. 2006). Integration of the flux in the SED over wavelength produces what we will refer as deduced L, and the application of nonrotating color - effective temperature relations to the SED produces what we will denote as deduced T_{eff}. Both these quantities will be strongly inclination dependent for sufficiently rapid rotation. There is also no straightforward relationship with the actual L (i.e. the total amount of energy coming out of the star per unit time) or the actual T_{eff}, which we define as $(L/(A\sigma))^{1/4}$ where A is the surface area of the star and σ is the Stefan-Boltzmann constant. Naturally the comparison between a computed SED and one observed has much prospect of success only if the inclination and the oblateness of the star are known. Fortunately important advances in interferometric instrumentation over approximately the last decade have permitted resolved observations of some nearby rapid rotators (e.g., van Belle et al. 2001; Domiciano de Souza et al. 2003; Aufdenberg et al. 2006; Monnier et al. 2007; Zhao et al. 2009; Che et al. 2011). The direct process requires performing the calculations with different models until the observed SED properties are matched to the extent possible. This can be laborious and it would be far preferable to be able to start with the observed SED properties and work backward to what the luminosity and the latitudinal variation of the effective temperature must be. A crucial first step in this process is to demonstrate that there is a well defined relation between the deduced quantities and their physically significant counterparts, even though this relation depends on both the inclination and the amount of rotation. We explore this relationship in this work.

Recently Deupree (2011a) showed that a number of properties of rotating models, particularly the surface effective temperature as a function of latitude, is proportional between models as long as the surface shape remains the same. Of course the surface radius as a function of latitude scales by definition. For the surface shapes to be exactly the same, the two models must have the same rotation law to within a multiplicative constant. The independence of latitude for the actual effective temperature and radius ratios suggests that observable properties such as the deduced luminosity and deduced effective temperature as functions of inclination may scale as well. If true, one might be able to at least place constraints on models and parameters which could produce the observed properties. It would also allow stepping backwards from the observed properties to the actual luminosity and effective temperature in a straightforward way for cases in which both the inclination and surface shape are known. Being able to reduce the uncertainty in a star's actual properties is important in determining whether differences between observed and computed oscillation frequencies are due to not having a model with the correct actual properties or not having the interior model structure right. This is very timely because the discovery of multiple oscillation frequencies in rapidly rotating stars such as α Oph (Monnier et al. 2010) for which interferometric observations (Zhao et al. 2009) have been made provides our best opportunity at the moment to study in detail the interior structure of rotating stars (e.g. Deupree et al. 2012; Mirouh et al. 2013).

We develop the model scaling relationships and discuss how the deduced properties scale in the next section. The following sections provide an example of how these scaling properties can be used and what are the limitations of the method.

2.2 SCALING PROPERTIES

We wish to examine the surface relationships between models which have the same surface shape. We assume that the surface is an equipotential, requiring the rotation law to be conservative. Some of the assumptions we make in the analysis hold for the laws we consider, and it is not clear what deviations from a conservative law are allowed before none of the scaling results hold. We shall return to this point in the final section.

2.2.1 Scaling of Model Properties

We first consider what scaling in this context means. Essentially, it means that for any surface variable of two models (y_1, y_2) with the same shape:

$$\frac{y_2(\theta_j)}{y_1(\theta_j)} = c_y \quad \forall \quad j \tag{2.1}$$

where θ_j is the co-latitude and c_y is a constant. This is true for the surface radius by definition.

Having the surface shape of two different models the same also imposes a number of conditions on those models. First, models that have the same surface shape have the same rotation law form, except for an overall scale factor:

$$\Omega_2(X_R, \theta_j) = c_\Omega \times \Omega_1(X_R, \theta_j) \quad \forall \quad j \tag{2.2}$$

where Ω is the rotation rate, c_Ω is a constant and $X_R = r_{R_1}/R_1 = r_{R_2}/R_2$.

The scaling of the rotation rate and the surface radius between two models with the same surface shape means the rotational velocities will scale as well. The scale factor can be determined from the ratio of the surface equatorial velocities of the two models. With both the rotational velocity and radius scaling, the centrifugal force scales as well.

Letting Φ denote the gravitational potential, we can write the total equipotential (Ψ) at the surface in the following way:

$$\begin{aligned}\Psi_1 &= \Phi_1(\theta) + \Omega_1^2(\theta)R_1^2(\theta)\frac{\sin^2(\theta)}{2} = \frac{\Psi_2}{c_\Psi} = \frac{1}{c_\Psi}\left[\Phi_2(\theta) + \Omega_2^2(\theta)R_2^2(\theta)\frac{\sin^2(\theta)}{2}\right] \\ &= \frac{1}{c_\Psi}\left[\Phi_2(\theta) + c_\Omega^2 c_R^2 \Omega_1^2(\theta)R_1^2(\theta)\frac{\sin^2(\theta)}{2}\right] \qquad (2.3)\end{aligned}$$

Given that the gravitational potential will have only a small nonradial component, we see that this equation can be solved only if both terms are true individually. Thus,

$$\Phi_2 = c_\Psi \Phi_1 \text{ and } c_\Psi = c_\Omega^2 c_R^2 \qquad (2.4)$$

We see that the gravitational potentials scale as well. To the extent one can approximate the gravity at the surface by the Roche potential (which one can do quite well for all but the most rapid uniformly rotating models), one can obtain an estimate for the mass once we know the appropriate scaling constants.

Deupree (2011a) has shown that scaling as defined in equation (2.1) is true for the effective temperature for ZAMS models from 1.875 to $8M_\odot$ with twenty different shapes. These effective temperature ratios appear to show a maximum variation of 0.5% over all latitudes. A part of the variation could be due to the fact that radii are discretized in the 2D finite difference mesh - a zone is either inside the model or it is not. The surface at each latitude is taken to be the outer radial boundary of the zone which the equipotential that describes the surface passes through.

We can see why the the effective temperatures might scale by application of von Zeipel's (1924) law to two rotating homologous models which have the same shape. This means that the equipotential surfaces will have the same shape at the same fractional radius. Because the flux, assumed to be radiative, is perpendicular to the equipotential surface, one has

$$\left[\frac{F_\theta(X_R,\theta_j)}{F_r(X_R,\theta_j)}\right]_1 = \left[\frac{F_\theta(X_R,\theta_j)}{F_r(X_R,\theta_j)}\right]_2 \tag{2.5}$$

where the subscripts 1 and 2 refer to the two models. This means that the same fraction of the flux is being diverted from the radial direction for each of the two models. If this is true at all locations inside the model, then the distribution of the flux emerging from the model outer boundary must have the same relative distribution with latitude in both models. Because the effective temperatures are defined in terms of the flux emitted from a surface zone, the effective temperatures of the two models must scale, satisfying equation (2.1).

We can also obtain this result from the work of Espinosa Lara & Rieutord (2011) , which finds that one may write $T_{\rm eff} = a\, g_{\rm eff}^{\beta}$, where β decreases slightly as the model becomes more oblate. Because $g_{\rm eff}$ scales, then $T_{\rm eff}$ scales as long as one is comparing models that have the same shape as we are here. We thank the referee for this insight.

Given sufficient information, one could expect to compute the latitude independent ratios of the surface radius, effective temperature, surface rotation velocity, and effective gravity. While these results may be of some theoretical interest, they would be more beneficial if properties obtained from observations, i.e. the deduced T_{eff} and deduced L, also scaled.

2.2.2 Scaling of observed properties

Two key variables one wishes to obtain from a star are the actual T_{eff} as defined above and L. This remains true for rotating stars, with the complication that neither the temperature nor the luminosity one would deduce from observations of a rapidly rotating star directly relate to intrinsic stellar properties because the deduced properties are strongly inclination dependent (e.g.Collins & Harrington 1966; Hardorp & Strittmatter 1968; Maeder & Peytremann 1970; Gillich et al. 2008; Dall & Sbordone 2011). To obtain a deduced effective temperature and luminosity from a spectral energy distribution for a rotating star requires the same knowledge about reddening and distance as for a spherical star, so we assume that this transformation can be performed to some degree and will address obtaining the deduced luminosity and effective temperature from dereddened SEDs with a known absolute flux.

The computation of the deduced effective temperature and luminosity as a function of inclination requires several steps. First, we must have the surface properties of the model, which here we take from the suite of ROTORC (Deupree 1990, 1995) ZAMS models computed by Deupree (2011a). We note that these models force a relationship between the local effective temperature and the local surface temperature, unlike von Zeipel's law which assumes that the surface is an equipotential (and hence constant temperature) surface while the effective temperature can vary significantly from pole to equator. The net effect is that the ROTORC models have a flatter relationship between the effective temperature and effective gravity, closer to 0.2 instead of the 0.25 of von Zeipel's law. We note that the behavior and values of our exponent with increasing rotation are quite similar to those of Espinosa Lara & Rieutord (2011). Previous studies consistently find a lower value preferable (Monnier et al. 2007; Che et al. 2011; Claret 2012). Second, we must also have the intensities emerging from the surface for each member of a grid of stellar atmospheres. For the intermediate mass main sequence models we wish to explore, plane parallel model atmospheres are satisfactory. The model atmospheres are computed with the PHOENIX code (Hauschildt & Baron 1999), and the grid covers the range in effective temperature from 7500K to 11000K in steps of 250K and in log g from 3.333 to 4.333 in steps of 0.333. The spectrum was computed from the far ultraviolet to 20000Å, with minimum wavelength (wavelength interval) maximum wavelength = 600Å (0.005Å) 1500Å (0.01Å) 3000Å (0.015Å) 4000Å (0.02Å) 6000Å (0.03Å) 8000Å (0.04Å) 12000Å (0.06Å) 16000Å (0.08Å) 20000Å. These intervals were chosen to keep the resolution greater than 250000 below 8000Å and about 200000 above 8000Å. Lines in the four lowest ionization stages of Al, S, and Fe; in the three lowest of C, N, O, Mg, K, and Ca; in the two lowest of He, Li, and Na; and in the lowest of H and Ne are computed in NLTE. More specific details are given by Gillich et al. (2008) and Deupree et al. (2012). At lower temperatures than included we would need to include more species in NLTE, and at higher temperatures photometric temperature indicators in the visible region of the spectrum become harder to find. The net result of these two steps is that at any place on the surface of the rotating model, one can interpolate through the grid of model atmospheres in log T_{eff} and log g to obtain the emergent intensity in any direction with respect to the local vertical. The third step calculates the direction to the observer, and thus the angle of the observer with respect to the local vertical, at every point on the surface, and performs the weighted integral over all the contributions of the intensities from every point on the surface visible to the observer to obtain the flux the observer would see. This approach for the third step is rather frequently used (e.g.,Slettebak et al. 1980; Linnell & Hubeny 1994; Frémat et al. 2005; Gillich et al. 2008; Aufdenberg et al. 2006; Yoon et al. 2008; Dall & Sbordone 2011), and the specific details in our calculations are outlined by Lovekin et al. (2006). The final SEDs were obtained by using a 50Å wide boxcar filter. Because of this filtering and the fact that rotation does not affect the equivalent width, the Doppler shifts were not included in the flux integrals, making the flux calculation computationally "embarrassingly parallel". There is an option to include the Doppler shift when one wishes to compute specific line profiles with no filtering.

SEDs were obtained for uniformly rotating models for five masses (1.875, 2, 2.25, 2.5 and $3M_{\odot}$) and six different rotation rates characterized by flatness ($1 - R_{\rm p}/R_{\rm eq}$) values of 0.112, 0.134, 0.156, 0.180, 0.207 and 0.234. To give an idea of how much rotation this is in more conventional terms, we note that the surface equatorial velocities range from about 230 km s^{-1} to about 360 km s^{-1}. The most rapidly rotating model was chosen to keep the minimum effective temperature above 7500K, below which we would need to include other low ionization potential metals in NLTE. Models with slower rotation rates were not included because the pole to equator temperature variation was less than about 1000K. Some computed effective temperatures for the $1.875M_{\odot}$ models for the two most oblate calculations were below this lower temperature limit, and those models were not included. The SEDs were computed at ten equally spaced inclinations from pole on to equator on.

Both the deduced effective temperature and deduced luminosity were obtained from the computed SEDs. As expected, we found that B-V provided a good indicator of the deduced effective temperatures, using a NLTE PHOENIX model of Vega with the parameters of Castelli & Kurucz (1994) to calibrate the color indices. The deduced effective temperatures were obtained from the simulated (B-V) color using the (B-V) - effective temperature relation for the plane parallel model atmospheres with the Vega calibration. The gravity used for the (B-V) - effective temperature relationship for the rotating models was the effective gravity at the co-latitude which corresponds to the inclination angle. However, the variation in effective gravity between the equator and pole is only a little larger than a factor of two, which would lead to a maximum error in the effective temperature of about $\pm 100K$ based on a comparison of the change in the color – effective temperature relations with gravity for the plane parallel model atmospheres. The scaling should still be successful because the models at the same shape have the same effective gravity distribution.

The deduced luminosities were computed by integrating the computed flux over all wavelengths, including a Rayleigh-Jeans tail from the end of the calculated wavelengths to infinite wavelength, and multiplying the result by $4\pi d^2$, where d is an assumed distance to the model from the observer. Because the SED is inclination dependent, the deduced luminosity and effective temperature will be also. We also note that, because determining the gravity becomes part of the scaling algorithm if the inclination and shape are known, one can iterate the process to make the deduced gravity and the assumed gravity consistent.

We first turn to the deduced luminosities to determine how well they scale from one model with the same shape to another. For each model we divide the deduced luminosity at each inclination by the actual luminosity. The results are presented in Figure 2.1 for models with the ratio of the polar to equatorial radius of 0.82, the most rapidly rotating case for which the temperatures of all five masses fall within the range allowed. We see that the curves all have the same shape, but that the variation from pole to equator increases slightly as the mass increases, particularly at small inclination. While not perfect, the results in Figure 2.1 are sufficient to indicate that a reasonable determination of the intrinsic luminosity could be made given an observed luminosity, inclination, and polar to equatorial radius ratio (assuming uniform rotation), at least in the mass range covered.

For the deduced effective temperatures, we proceed in a manner similar to that used for the luminosity. Here the actual effective temperature, defined as the effective temperature obtained from the flux given by the actual luminosity divided by the total surface area of the model, plays the role that the actual luminosity played in the previous discussion. We take the ratio of the deduced effective temperature at each inclination divided by the actual effective temperature for each mass at a given shape. The results are shown in Figure 2.2. Again we see that the curves for different masses show the same form. Interestingly, the largest differences are shown for models seen equator on instead of pole on, except for the $3M_{\odot}$ model, whose ratio at low inclination is noticeably larger than that for all the other masses. This variation with mass for both the deduced effective temperature and deduced luminosity suggests that these might be analogous to homology transforms for realistic models of stars – it works well over a restricted mass range, but is not universal

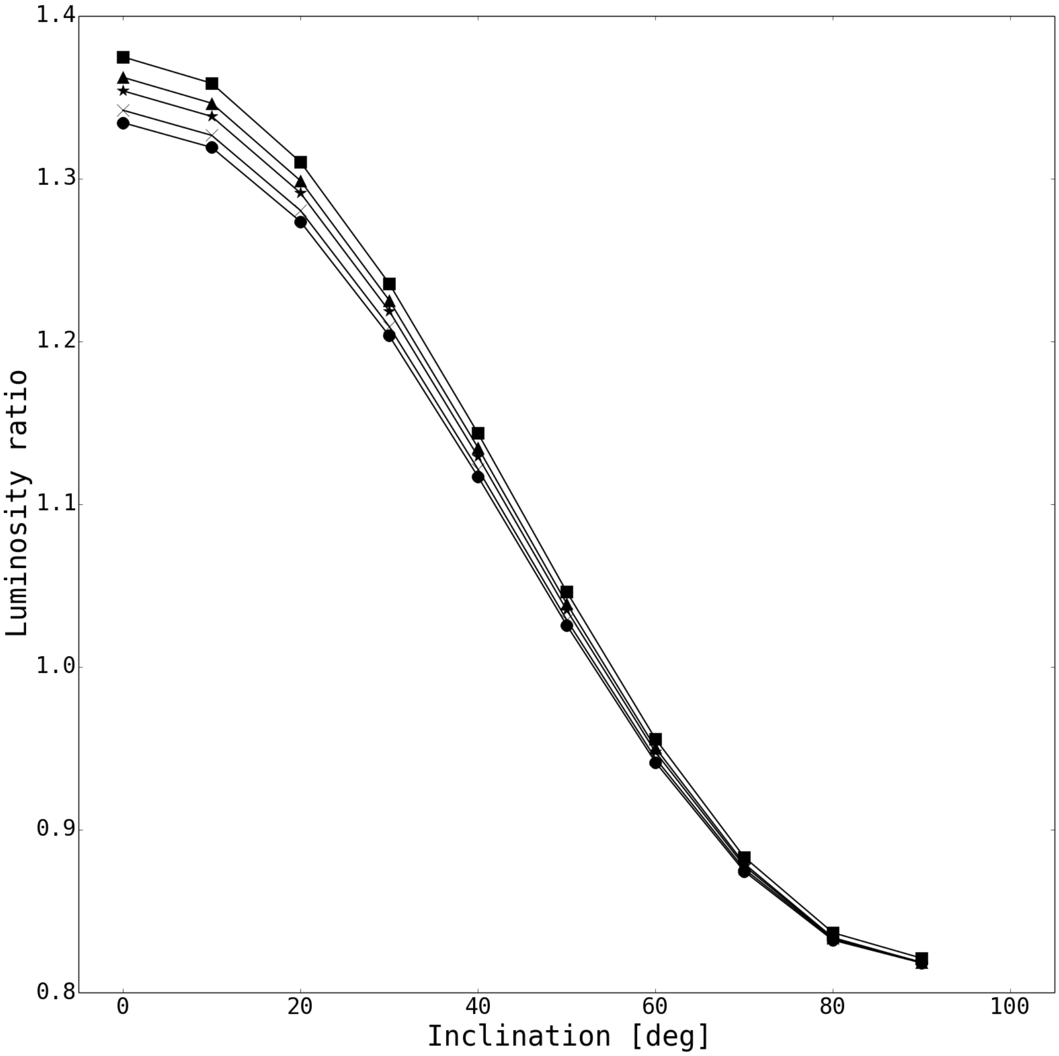

Figure 2.1: Ratio of the deduced luminosity to the luminosity as a function of inclination for ZAMS uniformly rotating models with masses of $1.875M_{\odot}$ (circles), $2M_{\odot}$ (crosses), $2.25M_{\odot}$ (stars), $2.5M_{\odot}$ (triangles) and $3M_{\odot}$ (squares). The ratio of the polar radius to equatorial radius is 0.82, corresponding to a surface equatorial velocity of about 300 km s^{-1}.

and progressively degrades as the physical properties of the models become less similar. It is worth mentioning that the ratio of the model effective temperatures at a given latitude for these masses does not show any significant latitudinal variation, so that the variation in the deduced effective temperatures must originate in the conversion from physical effective temperatures to observed ones.

Finally we consider whether the bolometric corrections deduced from these simulated SEDs are affected by any substantial changes rotation may introduce into the SED. This would be important if a full SED was not available. We computed the visual magnitude of our models and calculated M_V using the assumed distance. The visual magnitude was calibrated by scaling the flux of our spherical model for Vega to match the observed value above the earth's atmosphere at 5556Å (Hayes & Latham 1975) and then integrating the flux in the V filter and requiring $V = 0.03$ mag (Bessell et al. 1998). The absolute bolometric magnitude comes directly from the model luminosity with the bolometric magnitude of the sun set to 4.74. The bolometric corrections have been computed at inclinations between 0 and 90 degrees in ten degree intervals for all models. The results are shown in Figure 2.3, a plot of the bolometric corrections as a function of (B-V) for all inclinations of all models at all rotation speeds. Also shown in Figure 3 are the bolometric corrections for spherically symmetric models, the stars for $\log g = 4.333$ and the triangles for $\log g = 4.0$. Figure 3 indicates that the temperature is the key to the determination of the bolometric correction, but also that the effective gravity also plays a role (to about 0.07 magnitudes). Except through the effective gravity, rotation by itself does not appear to produce any particular modifications to the bolometric corrections for these models.

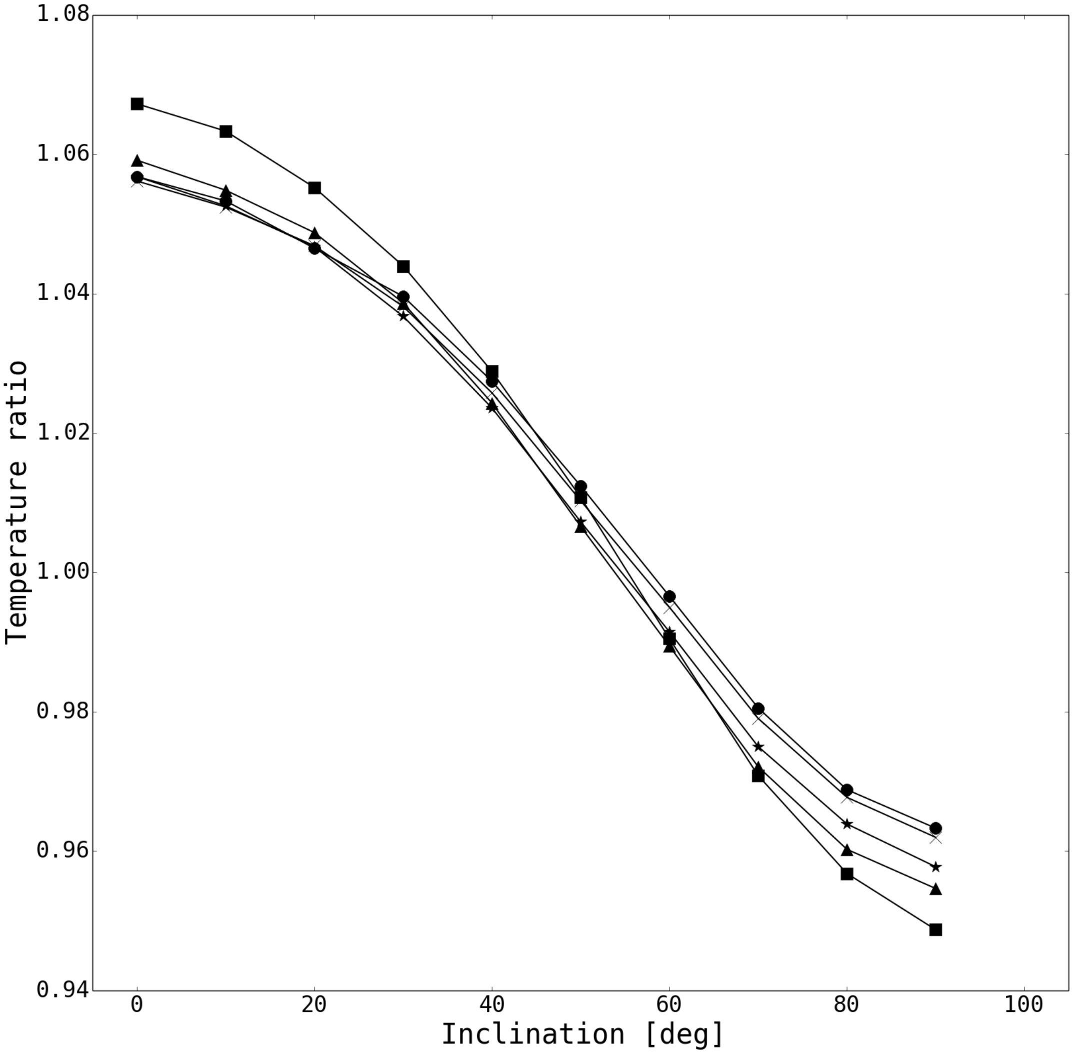

Figure 2.2: Ratio of the deduced effective temperature to the actual effective temperature (defined as the luminosity divided by the total surface area) as a function of inclination for the same models as in 2.1. Note the general agreement, although the results for the $3M_\odot$ suggest that there are limits to the applicability of the scaling.

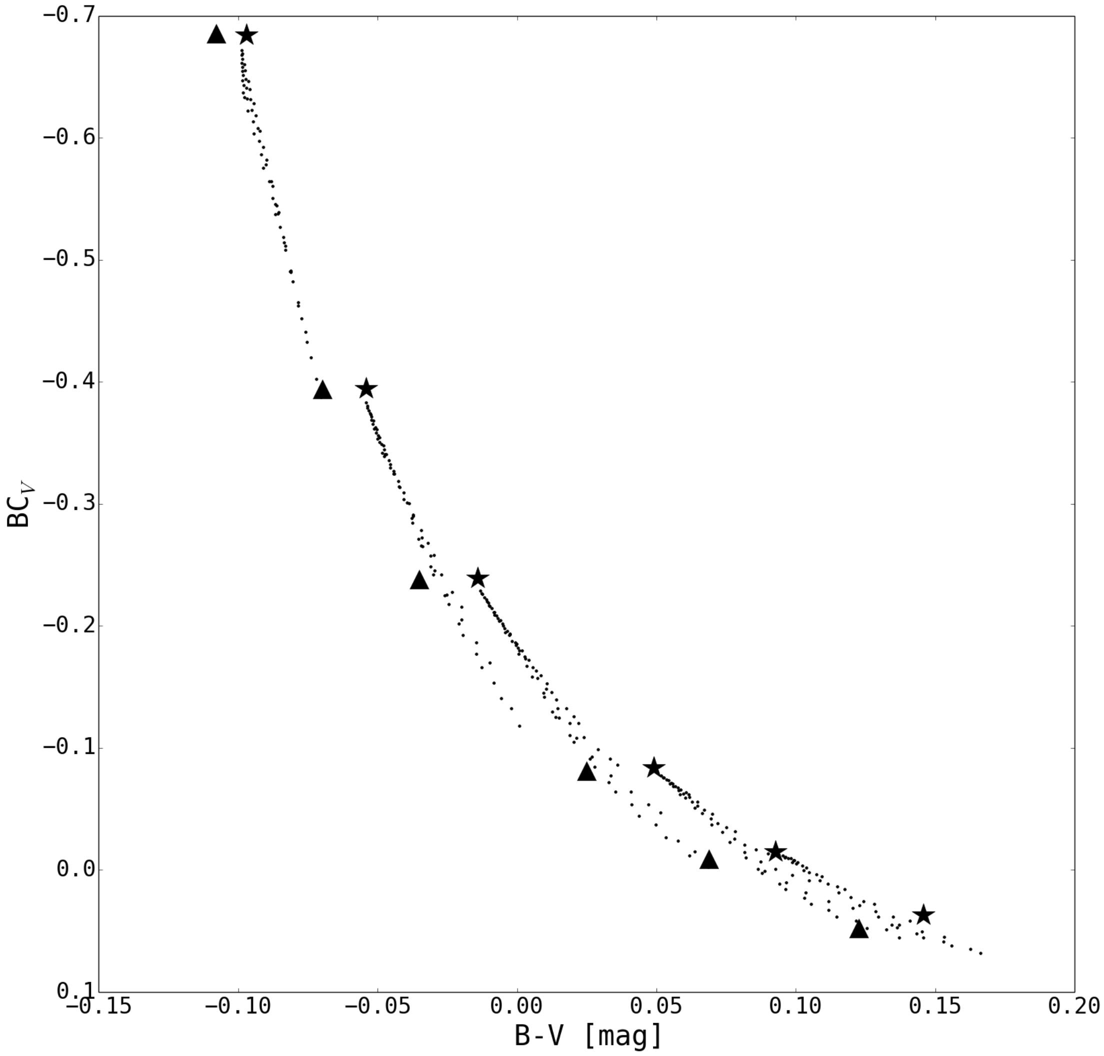

Figure 2.3: The dots show bolometric corrections for the SEDs of all models and inclinations. The stars denote plane parallel model atmospheres with $\log g = 4.333$ and the triangles denote those with 4.000. Note that the bolometric corrections are not significantly different between the rotating models and the spherical models.

Table 2.1. Model properties

Model	Mass ($M_\odot$)	$V_{\rm eq}$ (km/s)	Actual $T_{\rm eff}$ (K)	Actual L (K)
ZAMS 1	2.25	287	9474.5	25.48
ZAMS 2	1.85	237	8187.9	11.71
α Oph	2.19	229	8122.8	32.63

2.3 APPLICATION TO MODELS NOT ON THE ZAMS

The scaling relationship for deduced luminosities and deduced $T_{\rm eff}$ described above for the case of ZAMS models can be extended to models that are not in the same evolutionary state. To demonstrate this we consider a model of α Ophiuchus, a rapidly rotating A-type star. Interferometric observations of α Oph imply that it has a polar to equatorial radius ratio of 0.836 (Monnier et al. 2010) and Vsin i in the range of 210 - 240 km s^{-1} (e.g., Bernacca & Perinotto 1970; Abt & Morrell 1995; Royer et al. 2002). We compared this model with two ZAMS models which have the same shape as α Oph: one has a similar mass but different actual $T_{\rm eff}$ and the other with similar actual $T_{\rm eff}$ to α Oph but different mass. A summary of the properties of each model is given in Table 2.1. Using as input the deduced luminosity and effective temperature at a specific inclination from the α Oph model and applying the scaling relations to each ZAMS model allows the determination of the deduced effective temperatures and luminosities at all inclinations, the effective temperature as a function of latitude, and finally the actual effective temperature and luminosity for the α Oph model. We can then compare the results predicted by the two ZAMS models with those for the α Oph model itself.

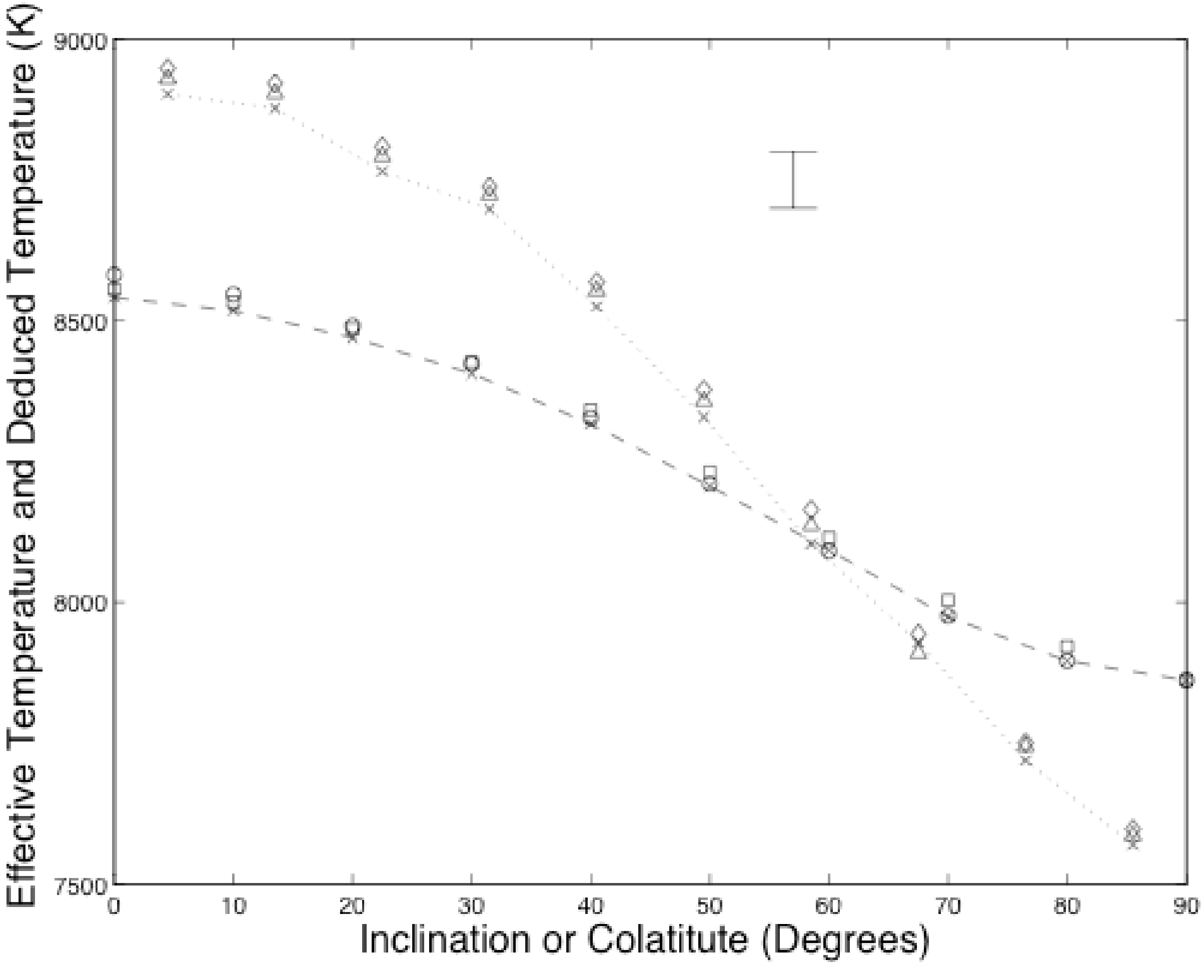

Figure 2.4: Plot of the effective temperature as a function of latitude (symbols on the dotted line) and the deduced effective temperature as a function of inclination (symbols on the dashed line). The diamonds, triangles, and crosses for the effective temperature refer to the results scaled from the $2.25M_\odot$ ZAMS model, the results scaled from the $1.85M_\odot$ ZAMS model, and the actual effective temperatures for the evolved model. The circles, squares, and crosses for the deduced effective temperatures refer to the results scaled from the $2.25M_\odot$ ZAMS model, the results scaled from the $1.85M_\odot$ ZAMS model, and the actual effective temperatures for the evolved model. A temperature range of $100K$ is also indicated and it is clear that all three temperatures agree with each other for all cases considered.

The comparisons of the deduced effective temperatures and actual effective temperatures are shown in Figure 2.4. We show the deduced temperatures as functions of inclination determined from the α Oph model (crosses), from the $2.25M_{\odot}$ model (circles), and from the $1.85M_{\odot}$ model (squares). Somewhat in keeping with the interferometric results for α Oph, we have chosen the deduced effective temperature and luminosity to be at an inclination of 90°. The latitudinal variation of the effective temperatures of the model is represented by the dotted line, and the variation of the deduced effective temperatues with inclination is shown by the dashed line. The same quantities are presented for the scaled $2.25M_{\odot}$ and $1.85M_{\odot}$ models. We note that in both cases each of the scaled two ZAMS models agree well with the actual model for α Oph. These results suggest that the precise details of the comparison model are not too important as long as the interior structures are sufficiently homologous. While "sufficiently homologous" is somewhat loosely defined, clearly these two models fit the requirements. On the other hand, one would not expect a $10M_{\odot}$ main sequence star to be an appropriate model for either α Oph or for a $10M_{\odot}$ red giant.

The result is the same for the deduced luminosity, as shown in Figure 2.5. Both ZAMS models scale well to the deduced luminosity for the α Oph model at all inclinations, although the $1.85M_{\odot}$ ZAMS model agrees with the α Oph model a little better. As one might expect from the agreement of these features, the actual luminosity and the actual effective temperature for each ZAMS model agree to within $0.12\,L_{\odot}$ and 40K with the value of the α Oph model.

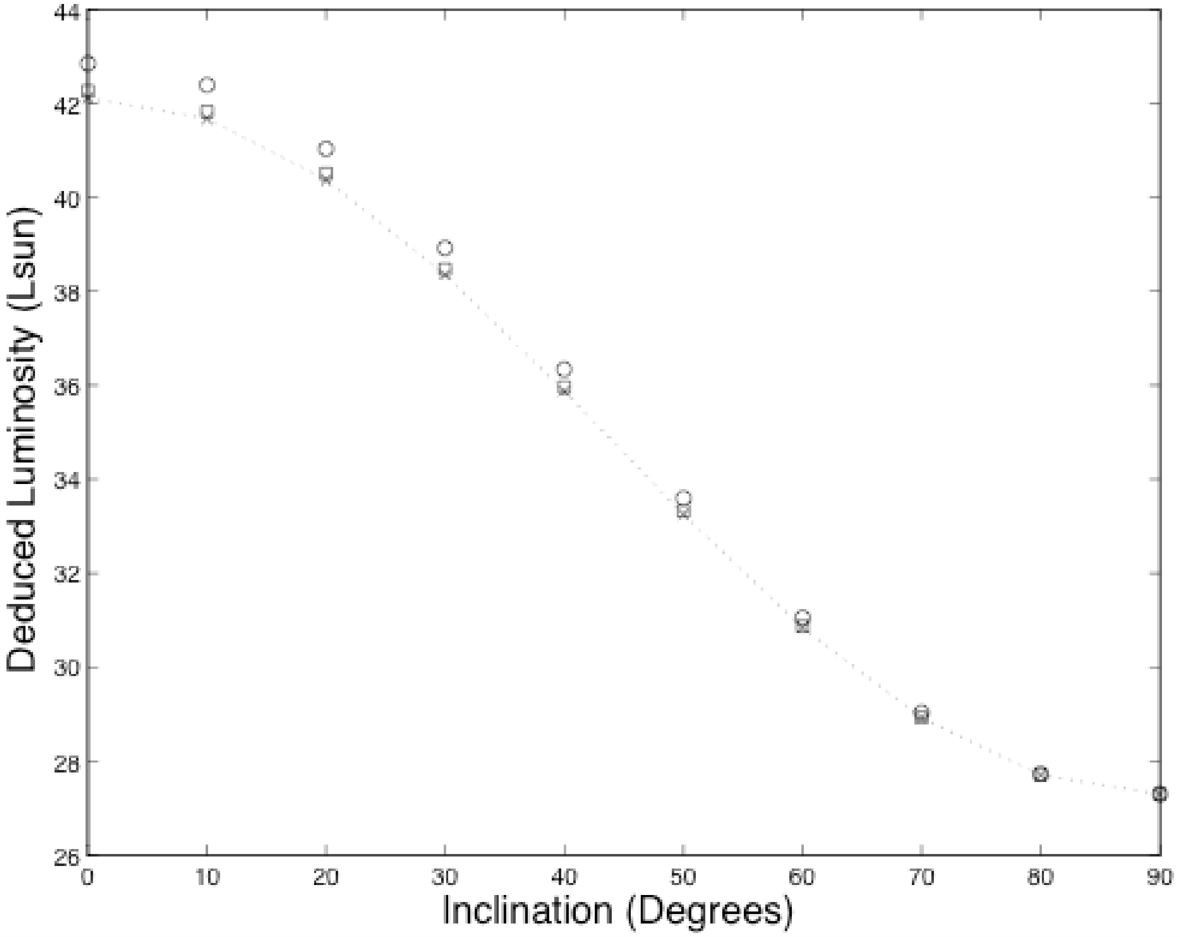

Figure 2.5: The deduced luminosity as a function of inclination for the evolved model based on the scaled $2.25M_{\odot}$ ZAMS model (circles), the scaled $1.85M_{\odot}$ ZAMS model (squares), and for the actual evolved model itself (crosses).

2.4 SCALING ALGORITHM

We have argued that the deduced luminosity and effective temperature scale for rotating models with the same shape over some limited range of conditions, and that this allows us to determine reasonable values for the luminosity and actual effective temperature of the unknown star from the models. Here we develop an algorithm to use the deduced and model scaling relations to obtain some intrinsic properties of a rotating star (for convenience, we shall refer to the rotating stellar models with known properties as the “model” and the unknown object whose properties we wish to obtain as the “star”) . We start by assuming that we have a deduced effective temperature, deduced luminosity, and a measurement of V$\sin i$. For the moment we assume that we also have the shape and inclination for the star as well. The reference model must have the surface radius, effective temperature, surface rotational velocity, and surface effective gravity as functions of latitude, the deduced effective temperatures and luminosities as functions of inclination, and the mass and luminosity of the model.

The algorithm proceeds as follows: from V$\sin i$ and the inclination of the star, compute the surface equatorial velocity, V_{eq}. Compute the ratio of the surface equatorial velocity of the model and the star. Because equation (2.1) is true for the surface velocity, one can compute the star’s surface rotation velocity at all latitudes. Because both the deduced effective temperatures and the latitudinal effective temperatures scale as shown in Figure 2.4, we have

$$\frac{T_{\mathrm{eff},1}(\theta_j)}{T_{\mathrm{eff},2}(\theta_j)} = \frac{T_{\mathrm{d},1}(i_j)}{T_{\mathrm{d},2}(i_j)} = \frac{T_{\mathrm{eff},a,1}}{T_{\mathrm{eff},a,2}} \quad \forall \quad j \tag{2.6}$$

here 1 refers to the model, 2 refers to the star, d refers to the deduced temperature, and a refers to the actual T_{eff} previously defined. Because the deduced temperatures are known at the inclination of the star for both the model (by interpolation) and the star (by observation), we can obtain the effective temperature at all latitudes and the actual effective temperature for the star. The actual luminosity of the star can be computed from the deduced luminosity at the assumed inclination, the deduced luminosity as a function of inclination for the model and the actual luminosity for the model. With the actual luminosity and actual effective temperatures known for both the star and the model, one can compute the ratio of the radii because the only difference between the surface areas of the model and the star is the difference in the radius. Hence, the radius of the star at every latitude of the star follows from the radius profile of the model.

The steps so far have depended only on the model, its deduced properties, and the scaling relations for both. These steps have resulted in the surface properties of the star as a function of latitude. The next step requires that the surface be an equipotential. As shown in Section 2.2.1, we use the fact that the gravitational part of the total potential and centrifugal potential must scale the same way for a given shape (i.e., at a given latitude, the ratio between the centrifugal potentials of the model and star and the ratio between the gravitational potentials of the model and the star must be the same). Because we have computed both the surface rotational velocity and the surface radius as functions of latitude for the star and have them for the model, we can obtain the ratio of the centrifugal potentials and hence of the gravitational potentials. Figure 2.6 presents a diagram of the information required from both the model and the star, as well as how the various unknowns of the star are determined from the scaling.

If we assume that the gravitational potential at the surface is given by that of a spherical star, at least at the equator, we can compute an estimate for the mass of the star. This assumption is generally good unless there is significant differential rotation where the material close to the rotation axis rotates much faster than the material farther away from the axis. It is certainly excellent for uniformly rotating models except those very near critical rotation (e.g., Ostriker & Mark 1968; Faulkner et al. 1968; Jackson et al. 2004; Deupree 2011a).

The reason for performing these last steps was to get an estimate of the mass which could be used with the actual luminosity to provide a check on the results. All the models utilized here are core hydrogen burning objects for which the main sequence mass - luminosity law should hold. A check on the reasonableness of the assumed inclination and shape can be made through how well the derived mass and actual luminosity fit the mass-luminosity law.

2.5 LIMITATIONS OF THE ALGORITHM

The scaling we have described relies on certain assumptions, and it is reasonable to see to what extent they can be relaxed. We have assumed that the surface is an equipotential, which only exists if the rotation law is conservative. Even for conservative rotation laws, it remains an assumption that the surface is an equipotential. This likely matters for the part of the solution that makes an estimate of the mass, but it need not affect the scaling of the observable properties as long as whatever mechanism determines the surface shape

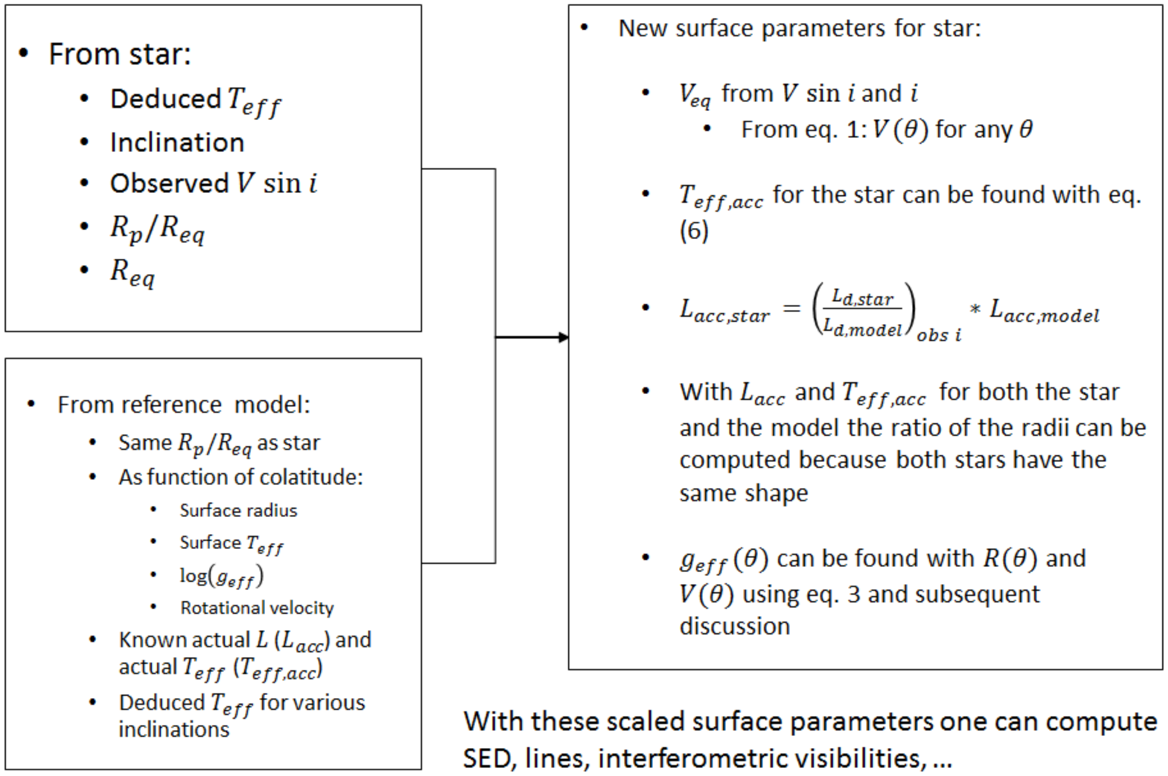

- From star:
  - Deduced T_{eff}
  - Inclination
  - Observed $V \sin i$
  - R_p/R_{eq}
  - R_{eq}

- From reference model:
  - Same R_p/R_{eq} as star
  - As function of colatitude:
    - Surface radius
    - Surface T_{eff}
    - $\log(g_{eff})$
    - Rotational velocity
  - Known actual L (L_{acc}) and actual T_{eff} ($T_{eff,acc}$)
  - Deduced T_{eff} for various inclinations

- New surface parameters for star:
  - V_{eq} from $V \sin i$ and i
    - From eq. 1: $V(\theta)$ for any θ
  - $T_{eff,acc}$ for the star can be found with eq. (6)
  - $L_{acc,star} = \left(\frac{L_{d,star}}{L_{d,model}}\right)_{obs\ i} * L_{acc,model}$
  - With L_{acc} and $T_{eff,acc}$ for both the star and the model the ratio of the radii can be computed because both stars have the same shape
  - $g_{eff}(\theta)$ can be found with $R(\theta)$ and $V(\theta)$ using eq. 3 and subsequent discussion

With these scaled surface parameters one can compute SED, lines, interferometric visibilities, …

Figure 2.6: Diagram showing representation of the scaling algorithm (see section 2.4). It shows the information required from both the model and the star, as well as how the various unknowns of the star are determined from the scaling are presented.

determines it in the same way for both the unknown and comparison objects. Our very limited knowledge of the surfaces of rotating stars does not allow an answer to this question.

We also assume that we know both the inclination and the surface shape of the unknown object. This in general is not true, and it turns out that there are combinations of inclination and shape which produce reasonable results, including masses which fit the mass-luminosity relation. The general trend is that more rapid rotation (i.e., more oblate shapes) can be offset by smaller inclinations. One might also add that determining the surface shape accurately potentially pays dividends by possibly placing constraints of the rotation law.

We have also used a single composition for all our models. A different composition would make a difference by producing a different color - effective temperature relation. We can obtain a crude estimate of how this might affect results by comparing the color-effective temperature relations of several spherical models at different temperatures with two different compositions. We calculated NLTE plane parallel model atmospheres with temperatures of 8000, 9000, and 10000K using half the metallicity of our previously computed models. The deduced temperatures for spherical models at these temperatures were all within 50K of the actual temperature when using the color-effective temperature relation from the full metallicity models.

These results lead us to believe that scaling of observables can be a useful technique to make the bridge between what one observes for rotating stars and physically useful information under appropriate conditions. We should caution that these results cover only a limited range in gravity and effective temperature and that extension far outside this range may not be warranted.

The authors thank Compute Canada and ACEnet for the computational resources used in this research.

Chapter 3

Scaling of oscillation frequencies in rotating stars

The contents of this chapter originally appeared as Castañeda, D. and Deupree, R. G. 2016, Monthly Notices of the Royal Astronomical Society, 458, 4422. They are reproduced here in accordance with the copyright policy outlined by the publisher (http://www.oxfordjournals.org/en/access-purchase/rights-and-permissions/publication-rights.html).

Properties of stars undergoing pulsation such as the well known root-mean-density scaling relation can be useful when trying to match the observed properties of a particular star. It is often assumed that this relation is valid for p mode frequencies in rotating stars. To

examine the change in frequency with rotation and mass, we have studied oscillation frequencies of two-dimensional uniformly rotating zero-age main sequence stellar models in the delta Scuti mass range. We identified axisymmetric *p* and *g* modes for non-rotating models and then traced them as the rotational velocity was increased. We considered a rotation sequence of ten models for four different masses, with the largest rotation rate being about 200 km s^{-1}. The models were required to have the same surface shape between all masses for a given rotation rate. We find that scaling relationships exist among the oscillation frequencies of the same mode for different masses when the models have the same shape. For p modes, this scaling closely follows the period root-mean-density relation found in spherical stars. The *g* modes also scale between models of the same shape, with the scaling reflecting the change in properties outside the convective core as the stellar mass increases. These scaling relationships can be particularly useful in finding specific stellar models to match the oscillation frequencies of individual stars. We also find that the large separation scales approximately with the root mean density as the rotation rate increases, although the individual mode frequencies do not.

3.1 Introduction

It has long been recognized that stellar oscillations provide a unique opportunity to study the interior structure of stars. Thanks to the space based missions MOST (Walker et al. 2003), CoRoT (Baglin et al. 2001), and Kepler (Basri et al. 2005), we now have accurate frequencies for a large number of stars, including intermediate mass main sequence stars such as the δ Scuti stars (e.g., Michel et al. 2008; Kjeldsen et al. 2010). While much effort has been expended modeling these stars (e.g., Templeton et al. 1997; Breger 2000; Suárez et al. 2014; Ouazzani et al. 2015), a global understanding of the fine structure of these stars still eludes us.

A significant complication for many of these stars is rotation. Very small rotation removes the degeneracy of the non-axisymmetric modes, but only modest rotation is required before the mode splitting is comparable to the large separation, complicating any analysis of an observed frequency spectrum (Suárez et al. 2010; Deupree & Beslin 2010). Not much more rotation is required before the splitting of the non-axisymmetric modes becomes nonuniform. Rotation also alters the frequencies of the axisymmetric modes (e.g., Saio 1981; Lignières et al. 2006; Lovekin & Deupree 2008). Finally, significant rotation deforms the star sufficiently so that the spectral energy distribution (SED) depends on the (usually unknown) inclination between the rotation axis and the observer, so that even placing the star in the HR diagram becomes nontrivial. The picture is brightened somewhat by the advent of optical interferometry, which allows us to determine both the inclination and, to some extent, the amount of rotation through the observed distortion of the stellar surface for a limited number of stars (e.g.,van Belle et al. 2001; Domiciano de Souza et al. 2003; Aufdenberg et al. 2006; Monnier et al. 2007; Zhao et al. 2009; Che et al. 2011).

For a rotating star the horizontal and radial variables of the perturbations in a linear pulsation analysis are no longer separable as they are for a non-rotating star. In effect this means that the latitudinal component of the eigenfunction can no longer be given by a single Legendre polynomial, but must be regarded as a sum of Legendre polynomials. This has led to two dimensional solutions to the eigenvalue problem (e.g., Clement 1998; Yoshida & Eriguchi 2001; Espinosa et al. 2004; Lignières et al. 2006; Lovekin & Deupree 2008; Lovekin et al. 2009; Ouazzani et al. 2012, 2015).

Under the best of circumstances the task, then, is to find a rotating model which has the observed oblateness and oscillation frequencies and which, when viewed at the observed inclination, produces the observed SED. Because the oblateness is tightly coupled to the mass, stage of evolution and the rotation rate, it is unreasonable to expect that just evolving rotating models from the ZAMS to the approximately right place in the HR diagram will satisfy all these conditions. Fortunately, we can simplify the process in various ways.

Deupree (2011a) computed a number of ZAMS models with different mass and rotation rates and found that any two models which have the same surface shape (close to having the same value of $\Omega/\Omega_{\mathrm{crit}}$ but not quite) have the same relative distribution of the effective temperature as a function of latitude. The effective temperature and effective gravity as a function of latitude and the surface shape are used to compute the SED that would be observed at a given inclination between the rotation axis and the observer (e.g., Slettebak et al. 1980; Linnell & Hubeny 1994; Frémat et al. 2005; Aufdenberg et al. 2006; Lovekin et al. 2006). This suggests that the deduced effective temperature and deduced luminosity, which one would obtain from the SED under the assumption that it originates from a spherical star, might have the same relative distribution as functions of the inclination as well. Castañeda & Deupree (2014) performed calculations of the SED and showed that this is the case as long as the models are not too dissimilar in structure (much like the period - root mean density relation applies).

Such scaling allows the determination of the surface conditions of a rotating star with relatively little computation. The scaling algorithm assumes that the oblateness and inclination of the star is known from interferometric observations and that there is access to a rotating model with the observed oblateness. Besides the surface properties of this model, the (computed) deduced effective temperatures and luminosities as a function of inclination are required. Also needed are the deduced effective temperature and deduced luminosity at the observed inclination of the star, which can be computed from the observed SED in the same way as they were computed for the model. With this information, the ratio between the surface properties and the deduced properties of the model and the observed star can be calculated, leading to all the surface and intrinsic properties for the rotating star. This is equivalent to placing a non-rotating star in the HR diagram. See Castañeda & Deupree (2014) for more details regarding the scaling process.

The next step is to compute a model that has the correct shape, surface effective temperature distribution, and total luminosity. Evolution tracks should get one close, and then one converges models with small perturbations to the rotation rate, total mass, and composition distribution to obtain the model. Of course, it is unlikely that this model will have the observed oscillation frequencies, so we must now make corrections to the model to improve the agreement between the observed and model oscillation frequencies. This can be most easily performed if there are scaling relations between the oscillation frequencies of two models, much like the conditions for which the period-root mean density relation for non-rotating stars, to guide us.

Previous studies have been able to relate properties of the oscillation spectra like the large separation with physical properties of the star, particularly the mean density (Reese et al. 2008; García Hernández et al. 2013; García Hernández et al. 2015) for stars close to the δ-Scuti range of masses. This is can be an important tool when trying to find patterns that can aid the mode identification process. In particular, Lovekin et al. (2009) tested physically meaningful radii that would make the period-mean density relation, $Q = P\sqrt{M/R^3}$, constant as the rotation rate increases. Using the radius at 40 seemed to keep Q constant as a function of the rotation rate, but its selection had no physically meaningful justification. For the models we are considering however, a natural consequence of comparing two stars with different masses but the same surface shape is that by definition their physical volume will be proportional between each other. Additionally, if the range of masses is small enough so that their internal structures are similar, this volume proportionality could potentially relate their oscillation properties directly, just like the period - root mean density scaling relationships for non-rotating stars. One purpose of this paper is to test the validity of this hypothesis. The mean density can be changed by at least three quantities associated with stars; the stellar mass, rotation, and evolution. With our models we can judge the relative importance of each in terms of scaling oscillation frequencies using the mean density

Section 3.2 presents the procedure followed to obtain the oscillation frequencies of the models considered. In Section 3.3 we present an overview of the modes found in the frequency range considered, mainly highlighting some of the challenges encountered while each mode was followed as rotation rate increased. Section 3.4 presents the results of what happens when the oscillation frequencies between two rotating models that have the same surface shape are compared. Section 3.5 discusses the relative importance of the stellar quantities that can affect the mean density. Finally section 3.6 contains a review of the results, potential applications as well as the limitations of the relationships found.

3.2 CALCULATION OF OSCILLATION FREQUENCIES

We follow the same procedure for calculating the oscillation frequencies of rotating stars used by Lovekin & Deupree (2008), Lovekin et al. (2009) and Deupree & Beslin (2010). The method is a two step process: First we use 2D rotating models calculated using the ROTORC code developed by Deupree (1990, 1995). The code solves conservation equations for mass, three components of momentum, energy and hydrogen abundance, as well as Poisson's equation for the gravitational potential. The particular models included in this work are all a subset of the models presented in Deupree (2011a); they are are zero-age main sequence (ZAMS) models with uniform rotation and solar metallicity with masses between 1.875 and 2.5 $M_{\odot}$, approximately covering the δ Scuti mass range. For each mass we picked ten surface equatorial rotational velocities, keeping $R_{\rm pole}/R_{\rm eq}$ of the model constant between the different masses at every step in rotational velocity. A summary of the properties of these models is given in Table 3.1. It is notable that the ratios between the polar and equatorial effective temperatures are effectively the same for all masses for a given ratio of polar to equatorial surface radius (Deupree 2011a). The effective temperatures at each latitude are not determined by von Zeipel's law, but rather are determined by a relation between the local effective temperature and local surface temperature. This makes $\partial \log g / \partial \log T_{\rm eff}$ smaller, closer to 0.2 than to the value of 0.25 given by von Zeipel's law. This smaller value is similar

Table 3.1: Rotating models considered

	Mass ($\mathrm{M}_\odot$)				
	1.875	2.000	2.250	2.500	
Shape ($R_{\mathrm{pole}}/R_{\mathrm{eq}}$)	Velocities ($\mathrm{km\,s^{-1}}$)				$T_{\mathrm{eff,pole}}/T_{\mathrm{eff,eq}}$
1.000	0.0	0.0	0.0	0.0	1.000
0.997	35.0	36.0	36.0	37.5	1.003
0.991	62.0	63.0	65.0	67.0	1.009
0.985	83.0	84.0	87.0	89.0	1.015
0.976	105.0	106.0	109.0	111.0	1.024
0.966	125.0	127.0	131.0	134.0	1.034
0.954	146.0	148.0	152.0	156.0	1.047
0.940	165.0	168.0	173.0	178.0	1.064
0.925	187.0	190.0	195.0	200.0	1.079
0.907	207.0	211.0	217.0	222.0	1.098

to that found in previous studies by various means (e.g., Monnier et al. 2007; Che et al. 2011; Espinosa Lara & Rieutord 2011; Claret 2012).

We calculated pulsation frequencies using the linear, adiabatic, non-radial pulsation code developed by Clement (1998). This code expresses the eigenfunctions of each mode as a sum of up to eight spherical harmonics with a radial resolution of 500 zones. In particular, for this study we calculated modes with ℓ values up to 15 (even and odd parity modes can be computed separately). The primary motivation for the number of basis functions is to obtain the frequencies of the low ℓ modes accurately, not to compute the highest ℓ modes. For this reason, we choose to include in our analysis only values of ℓ between 0 and 6. Similarly, we focus our discussion on the radial orders of p modes up to $n = 8$ in the non-rotating case because of our limited resolution near the model surface. We then follow these specific modes as a function of rotation, although we do take into account avoided crossings between the modes we are interested in and the higher ℓ modes. As was found by previous studies using this code (Lovekin & Deupree 2008; Deupree & Beslin 2010), we find that 8 spherical harmonics can yield accurate eigenfrequencies for selected modes and rotational velocities considered. Specifically we found that the difference in computed frequencies of modes using 6 and 8 basis functions is on average on the order of a few thousands of a percent for the lowest rotating models and about a tenth of a percent for the highest rotating models. These frequency differences indicate that at least for the modes selected, the number of basis functions is adequate.

For rapidly rotating stars the process of classification of modes is more problematic than for non-rotating stars. The major reason is because the usual latitudinal quantum number, ℓ, is no longer sufficient to specify the latitudinal variation of the eigenfunction. Similar to other studies, (e.g., Lignières et al. 2006; Lovekin & Deupree 2008; Lignières & Georgeot 2009; Deupree & Beslin 2010) we address this problem by characterizing each mode with the value of ℓ associated with the mode in the non-rotating model, ℓ_0. This tracing process, although useful, becomes progressively more difficult for more rapidly rotating models. For each model we identified the same combination of g and p modes as well as several radial modes. In total, we computed 180 modes with even parity and 189 modes with odd parity. Table 3.2 presents the non-rotating modes identified. Of these, the number of modes which match the analysis criteria described above is 78. Under the classification scheme developed by Lignières et al. (2006); Lignières & Georgeot (2009); Reese et al. (2009) in which modes for rapidly rotating stars can be separated as either island, whispering gallery or chaotic modes, we expect our selected low degree modes to be mainly island modes.

Table 3.2: Oscillation modes calculated for each model. The value of n denotes the number of radial nodes found in mode for the non-rotating case

ℓ	n-range (g mode)	n-range (f and p mode)
0		0-15
1	1	1-16
2	1-2	0-14
3	1-3	0-15
4	1-4	0-15
5	1-5	0-15
6	1-7	0-15
7	1-8	0-14
8	1-9	0-13
9	1-10	0-13
10	1-11	0-13
11	1-13	0-13
12	1-13	0-12
13	1-15	0-12
14	1-16	0-12
15	1-18	0-12

3.3 VARIATION OF MODE FREQUENCIES WITH ROTATION

Significant research has been performed to determine the behavior of oscillation frequencies with rotation. Some studies have used the "traditional" approximation in which the horizontal component of the angular momentum is neglected in the linearized momentum equations (e.g., Lee & Saio 1986, 1997; Townsend 2003). Two other prominent methods are perturbation techniques (e.g., Saio 1981; Dziembowski & Goode 1992; Soufi et al. 1998; Suárez et al. 2010) and, in principle the more reliable, numerical integrations with the horizontal variations assumed to be given by a sum of spherical harmonics (e.g., Clement 1998; Lignières et al. 2006; Lovekin & Deupree 2008; Ballot et al. 2010). Other studies have also explored the problem using ray theory principles (e.g, Dintrans & Rieutord 2000; Lignières & Georgeot 2009; Pasek et al. 2012; Prat et al. 2016) to compute oscillation frequencies in the asymptotic regime. Here we use Clement's radial finite difference integration approach in the radial direction. Furthermore, we will consider only axisymmetric modes. We shall distinguish different latitudinal modes by "ℓ", even though the modes are actually linear combinations of different ℓ's. When we use a specific value of ℓ, we intend this to mean the value to which a given mode could be traced back to at zero rotation. Figure 3.1 shows the general evolution of oscillation frequencies with rotation. The p mode frequencies decrease, mostly because the stellar volume increases, and hence the mean density decreases, with rotation. The g modes, on the other hand, generally increase in frequency as the rotation rate increases (e.g., Ballot et al. 2010), but by a much smaller amount. This figure also shows a subset of low radial order g modes that increase in frequency with increasing rotation at low rotation, but then begin to decrease with frequency as the rotation increases further.

To discuss these and other features, we divide the frequency range covered into four intervals: 1) low frequency which is defined as having only g modes, 2) an intermediate frequency region which includes both g and p modes, 3) a higher frequency region which includes only p modes, but at frequencies sufficiently low that there are still sizable variations in the frequency difference between radial quantum numbers n and n+1 for different latitudinal modes, and 4) the high frequency regime in which the large separation is essentially the same for all latitudinal modes. We shall address each of these frequency regions in turn.

The low frequency g modes in our set are perturbed much less by rotation than the p modes for the uniformly rotating models. This is because the g mode frequencies are most sensitive to the region just exterior to the convective core boundary while the rotational effects on the model structure are substantial only near the surface. Both the frequencies and the eigenfunctions in this interval are modestly perturbed, making mode identification relatively easy. The change in frequency from the non-rotating value for a given rotation rate is larger at lower frequencies, increasing by about 40% as the frequency is decreased by about a third. There seems to be little dependence with ℓ. This means that avoided crossings are rare, but they are not entirely absent. It would appear that a necessary condition is that the g mode frequencies are already quite close in the non-rotating model. Interestingly, previous studies (e.g., Ballot et al. 2012; Takata & Saio 2013) have found that some of these g modes with frequencies close to each other show particular rosette pattern in their internal structure. It is still not clear whether these modes are excited in real stars but we can confirm that some rosette modes are part of our data set. Figure 3.2 shows an example of one case found in our sample, in which a g mode with $\ell = 3$ and $n = 3$. The frequency evolution of these modes, however, does not seem to differ from the non-rosette modes, making them only interesting in their internal structure. Finally, we note that even our lowest frequency modes are somewhat above the sub-inertial range (thereby limiting the impact of the Coriolis force) and that the difference between their pulsation frequencies and the corresponding non-rotating values increases as the square of the rotation rate, reflective of the centrifugal force.

The region in which there are both p and g modes is the most complex. This region is relatively small in frequency width (the width increases as the rotation rate increases), but the mode density is relatively high and the different signs of frequency change for the p and g

modes with increasing rotation make near resonances and avoided crossings comparatively common. We present an example of avoided crossings in Figure 3.3 and also note from Figure 3.1 that the first p mode shows a change in its frequency evolution trend caused by one of these avoided crossings. Avoided crossings are relatively more common at higher ℓ because higher ℓ g modes for a given n have higher frequencies. Similarly, they are more common at lower n because lower n g modes have higher frequencies.

It is also in this interval that we see the phenomenon mentioned above where a given g mode frequency increases with increasing rotation up to a point and then decreases with further rotation (see Fig. 3.1). These are mixed modes that have nodes in the interior where the g mode nodes are expected and also much nearer the surface where p mode nodes occur (e.g., Scuflaire 1974; Osaki 1975). The frequency may actually begin to increase with increasing rotation before the node near the surface appears. This is similarly indicated in phase diagrams, such as defined by Scuflaire (1974) and Osaki (1975), in which the latitudinal displacement or, equivalently, $\frac{P'}{\rho} + \psi'$ (the primes denote Eulerian perturbations) is plotted against the radial displacement. The latitudinal displacement and the pressure-gravity perturbation are functionally equivalent in a non-rotating model, but not in a rotating one. We use the Eulerian pressure-gravity perturbation in part for convenience and in part because of the similarity of the latitudinal variation of this perturbation and the radial displacement. The phase diagrams are computed along radial lines (i.e., at a given latitude). At low rotation rates the phase diagrams at different latitudes show essentially the same clockwise or counterclockwise behavior, but the values of neither variable are the same. This is most noticeable at the surface, where the final point on the diagram may end in different quadrants for different latitudes. At higher rotation rates there may be different numbers of nodes at different latitudes, and in the phase diagram this may appear as loops which do not quite cross one or the other axes at some latitudes but do at other latitudes or as a direction reversal which crosses an axis for some latitudes but stops short of crossing at others. The relationship between the number of nodes and a specific mode identification becomes more murky at the highest rotation rates we use, although the motion in the phase diagram is still clockwise for g mode behavior and counterclockwise for *p* mode behavior with the type of mode behavior determined by where the nodes are in radius. The change of the phase diagram with rotation for a mode that will become mixed as the rotation rate increases is as follows. As the radius increases, the curve proceeds in a clockwise direction for *g* modes, but for these *g* modes that show a frequency decrease with increasing rotation, the motion becomes counterclockwise at sufficiently large fractional radius, although it does not continue far enough to produce a node near the surface. Because the effect increases as the rotation rate increases, one expects that *p* nodes will appear at yet more rapid rotation. We do see f modes that are mixed in these non-rotating ZAMS models, and adding rotation eventually leads to eigenfunctions in which the node pattern is more pronounced. Rotation also extends mixed modes to some low radial order *g* modes. There may be an avoided crossing before this mixed original *g* mode occurs.

Avoided crossings also occur in the third frequency region where there are no *g* modes. The usual case is a low latitudinal order *p* mode decreasing its frequency with increasing rotation reaching the frequency of a higher latitudinal order *p* mode that is decreasing its frequency more slowly with increasing rotation. Some easily identifiable crossing in our models appear to involve $\ell = 0$, 4, 8, although other cases certainly occur, in agreement with the crossing pattern found by Lignières et al. (2006). We show one such progression in Figure 3.4. The internal structure illustrations on the right show how it is still fairly easy to differentiate between the two modes involved after the interaction.

The final frequency interval is where n is sufficiently high that the large separation is virtually the same for all ℓ values. Thus, one has as many modes as one has spherical harmonics within a frequency interval given by the large separation. The large separation decreases very slightly with increasing rotation, as was found by Lignières et al. (2006) and by Lovekin & Deupree (2008). Another feature is that the eigenfunction for a given ℓ no longer changes very much from one value of n to the next for a given latitudinal mode. It was hoped that this frequency regime would be useful in mode identification, but the placement of modes within the large separation, including the ordering, may be different from one rotation rate to the next. For higher frequency modes techniques like the application of ray tracing methods have been successful at finding insights into the frequency patterns that could help their classification (e.g., Lignières & Georgeot 2009; Pasek et al. 2012). These methods, however, do not replace the need for highly resolved two dimensional calculations that provide more exact eigenfrequencies and eigenfunctions.

It is interesting to note that the trends for these intermediate mass ZAMS models are similar to those of the 10 $M_\odot$ model of Lovekin & Deupree (2008) and the rotating polytropic models of Lignières et al. (2006).

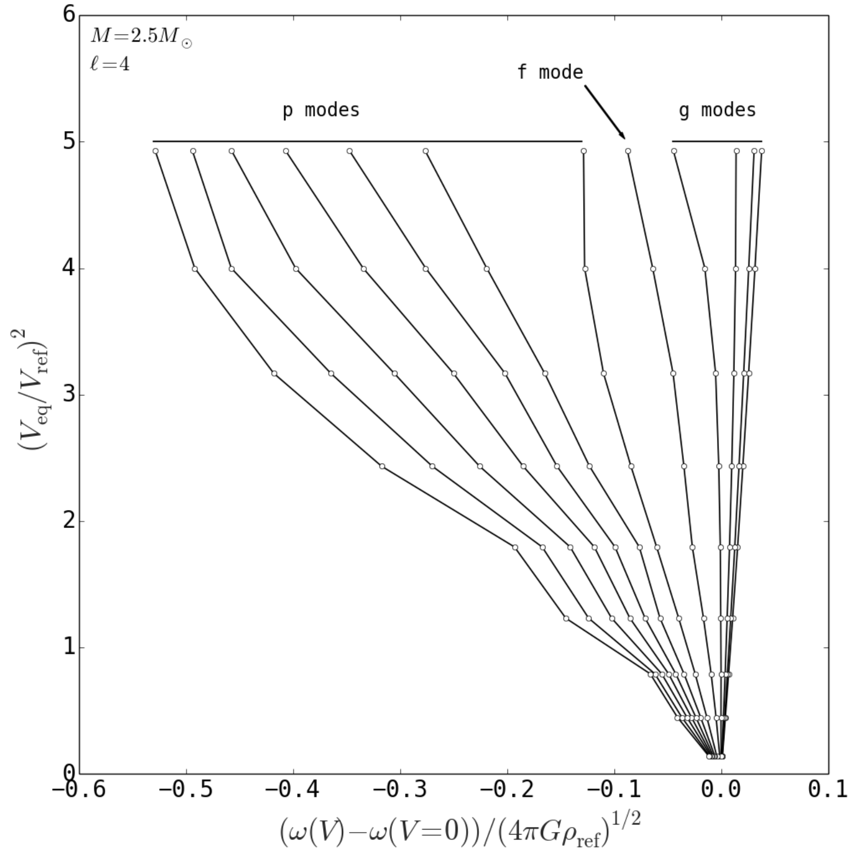

Figure 3.1: Rotational evolution of $\ell_0 = 4$ mode for $M = 2.5\mathrm{M}_\odot$. Frequencies are scaled by the factor $(4\pi G\rho_{\rm ref})^{1/2}$, where $\rho_{\rm ref} = 1\,\mathrm{g\,cm^{-3}}$, to keep their values at around unity across models and $V_{\rm ref} = 100$ km s^{-1}. Some of the changes in direction, most evidently for the first p mode, are caused by interactions with other ℓ modes as well as changes of properties of each mode as rotation is higher. Radial order increases to the left for the p modes and to the right for the g modes

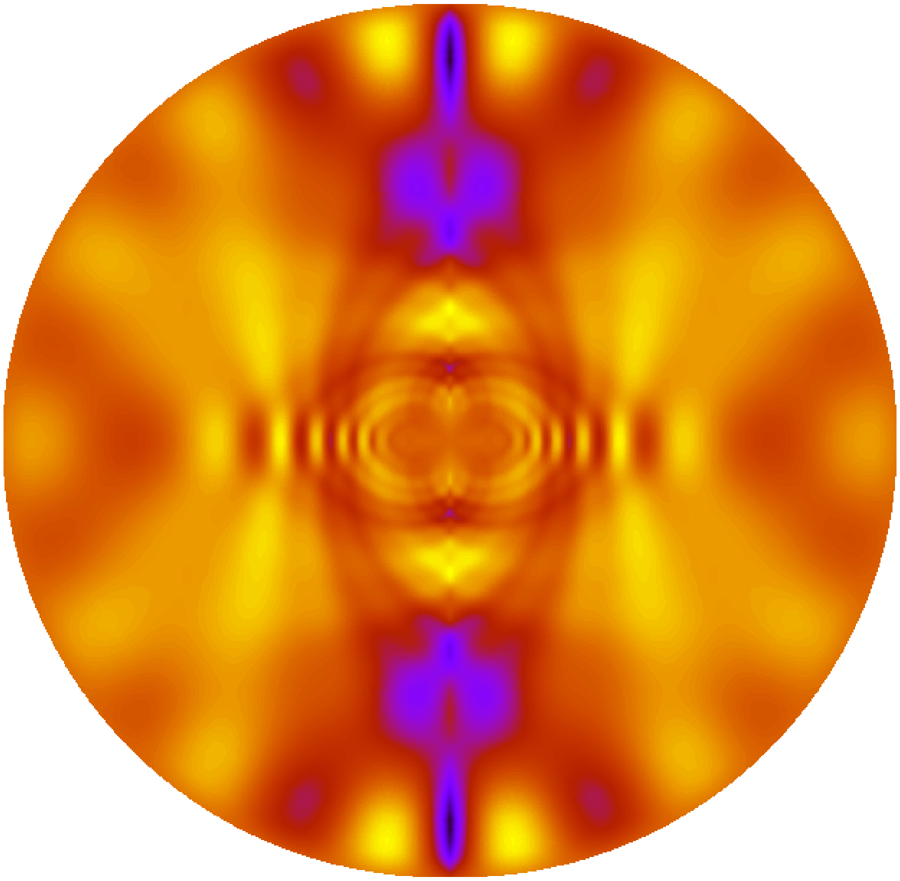

Figure 3.2: Meridional cross section of the pressure perturbation of a g mode ($\ell = 3$, $n = -3$) showing the rosette-like structure. A colour version of this figure is available online

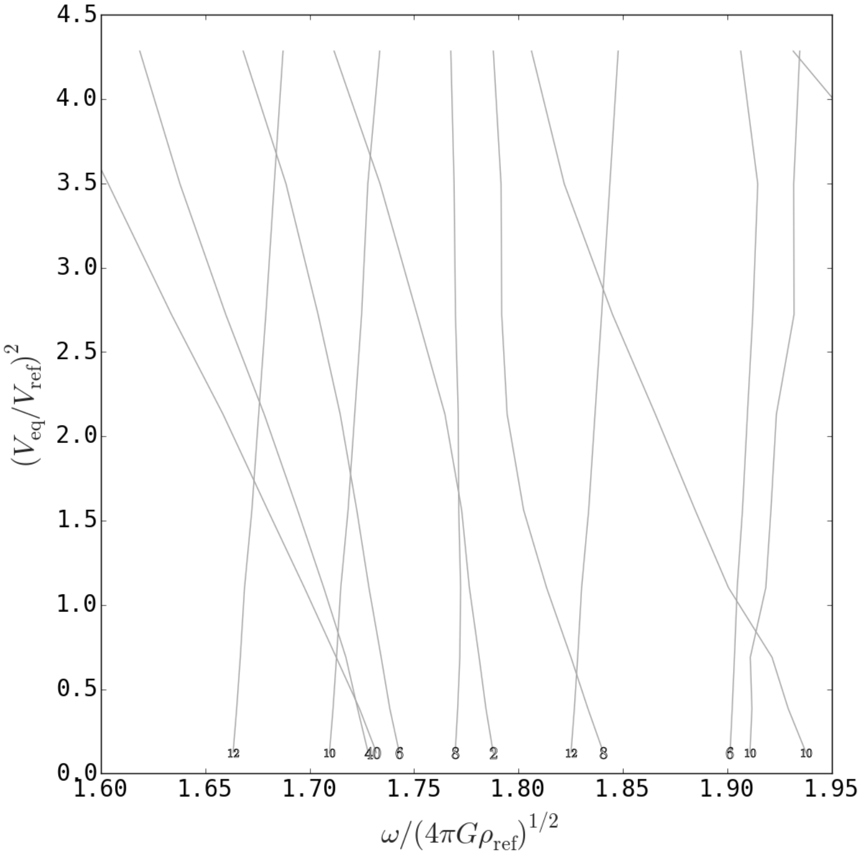

Figure 3.3: Rotational evolution of ℓ's with even parity calculated for the $1.875M_\odot$ models. $V_{\rm ref}$ and $\rho_{\rm ref}$ are as defined in Figure 1. We have labeled each line with its corresponding "initial" ℓ. There are a few cases of interaction between p modes whose frequency decreases as rotation increases and g modes whose frequency evolution behavior is the opposite. It is important to note that the lines do not cross, they correspond to avoided crossings. Modes in this region are the hardest to follow because in some cases modes can interact with each other two or three times before reaching the most rapidly rotating models included.

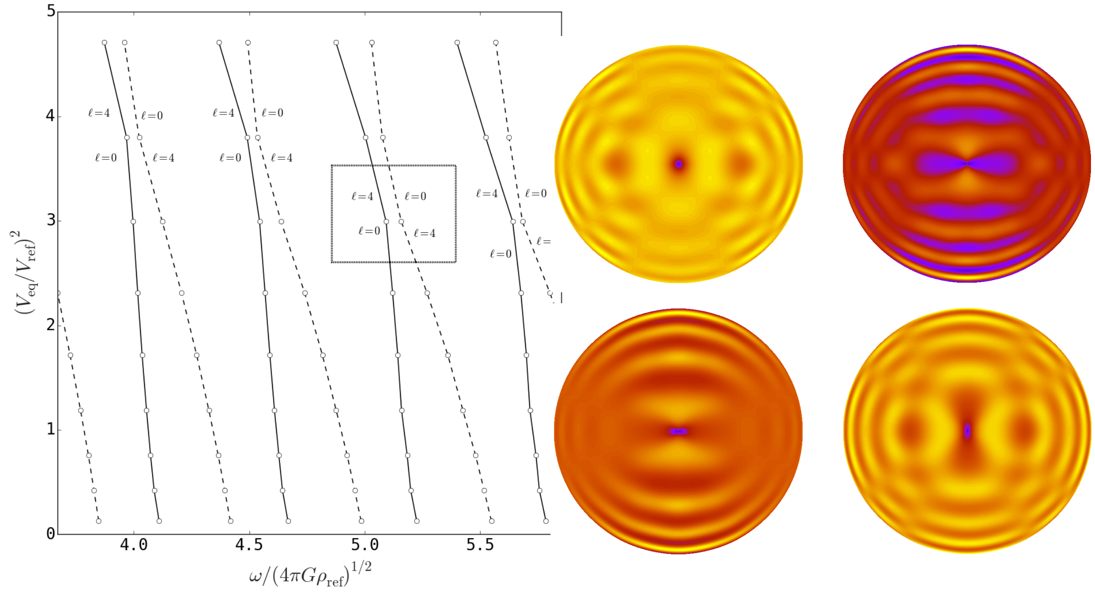

Figure 3.4: Mode interaction between modes with $\ell_0 = 0$ and $\ell_0 = 4$ for models of mass $M = 2.25\mathrm{M}_\odot$. $V_{\rm ref}$ and $\rho_{\rm ref}$ are as defined in Figure 1. It is possible to see the change in "label" required to match the exchange of surface latitudinal variation for each mode. The 2D contour plots on the right show the before and after of the meridional cross section of the pressure perturbations of the interacting modes enclosed in the box. In the case of the pressure perturbations, the lower frequency mode is on the left.

3.4 VARIATION OF MODE FREQUENCIES WITH MASS

The period-root mean density relation has long been a tool for scaling the oscillation frequencies or, alternatively, estimating the mean density for a model or star for which there is an object sufficiently similar in properties to make the comparison. It has often been tacitly assumed to remain useful for rotating stars. Strictly speaking, one can only expect it to be applicable to *p* modes, and our discussion about the different behavior of *p* mode and *g* mode frequencies with rotation suggests that the period-root mean density law does not apply for *g* modes. Here we will determine the applicability of the period-root mean density law for *p* modes of rotating stars and examine the scaling of *g* modes.

Figure 3.5 presents the frequency ratio of the same modes for the ZAMS models of 2 and 2.25 $M_\odot$. Figure 3.5 (left) shows the results for non-rotating models and Figure 3.5 (right) shows the same calculations for moderately rapidly rotating models. In each case the ratio of the two root mean densities is shown by the horizontal line. It should be noted that the two rotating models having the same surface shape means that the scaling of the stellar volumes will be exact and given by the cube of the ratio of the equatorial radii. It is clear that the effect of rotation on the *p* mode ratios is rather small and that the period-root mean density is still a useful indicator of how to change the model to obtain desired period changes.

It is also clear that the *g* modes do not follow this rule, although the ratios also do not depend very much on rotation. We can perhaps obtain some insight into how this *g* mode ratio comes about by applying equation (A13) from Tassoul (1980) to the stable g modes with radial nodes located between the outer boundary of the convective core and the surface ionization regions

$$\omega = \frac{(\ell(\ell+1))^{1/2}\int_{r1}^{r2} N\frac{dr}{r}}{(n+1/2)\pi - \theta_1 - \theta_2} \tag{3.1}$$

Here N is the Brunt-Vaisala frequency, and the thetas are phase shifts which occur if either N or the density or their derivatives are discontinuous at the limits of the integration. Because N is taken to be identically zero in the convective core, its first derivative may be discontinuous at the convective core boundary. The integral is taken between two radial locations which are consecutive zeros of N, in this case the convective core boundary and the lower boundary of the second helium ionization region. Assuming that we have successfully identified the same mode and the phase shifts are the same for each of the two models, the ratio of the two mode frequencies will be

$$\frac{\omega_a}{\omega_b} = \frac{\int_{r1a}^{r2a} N\frac{dr}{r}}{\int_{r1b}^{r2b} N\frac{dr}{r}} \tag{3.2}$$

Performing the integrations with the two non-rotating models in Figure 3.5, we obtain a ratio of 1.088, clearly close to the upper limit for the ratios of the linear, adiabatic frequencies. For all masses, the largest contributions to the integrals come from the region exterior, but relatively close, to the convective core. This is true both because N is relatively large and r comparatively small there. However, the contributions all the way out to the bottom of the second helium ionization region are not entirely negligible, even if less prominent than the deeper regions.

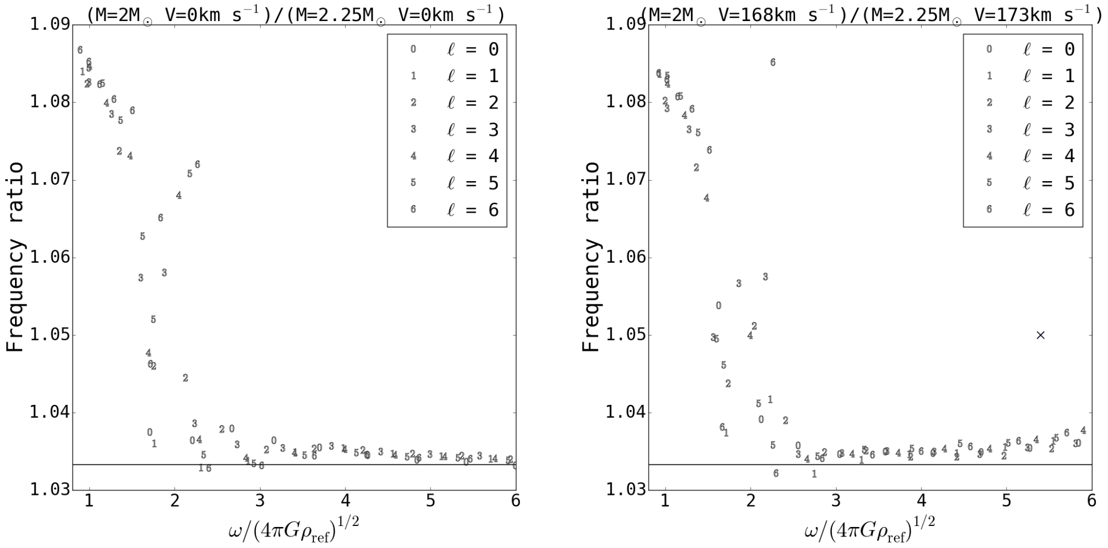

Figure 3.5: Ratio between frequencies of stellar models with the same shape. Left presents the non-rotating case. Right shows the same ratio for two rapidly rotating models. The black horizontal line indicates the ratio between the root-mean densities of both models. The cross shown on the figure of the right indicates what the ratio between modes that have undergone an avoided crossing for one mass but not the other. See the text for more details.

We also found that as rotation rate increased some of most interesting individual mode ratios were found in the frequency region that contains both *p* and *g* modes. For the non-rotating models, the modes with erratic ratio behavior with rotation are either the *f* mode or low radial order *g* modes, with no particular preference in latitudinal order. However, mode ratios in this region become significantly more complex with rotation. The ratios of some of these modes change very little with rotation, while the ratios for others change significantly. While no one feature accounts for the modes whose ratio changes significantly, modes bumped, modes with near resonances, and mixed modes appear to be more likely to display this behavior than others. The order at which modes appear in the non-rotating case in this region also seems to be different for every mass and can can also account for the erratic frequency ratio behavior. For the non-rotating cases about 12-18 modes out of the about 140 modes in this region, including all ℓ values, change places. Most of the modes involved in this ordering change, however, are modes with $\ell > 8$ and not taken into account for the ratio analysis.

We also see from Figure 3.5 that the ratios do not change significantly as rotation is included (except as we have indicated), at least up to the rotation rates presented here. We suggest that one may use the period-root mean density relationship for p modes in rotating models with the same reliability and constraints as one uses it in non-rotating models. The lower frequency g modes also scale predictably; it is only the modes in this intermediate region which are less predictable.

Finally note that in Figure 3.5 we have followed the mode frequency evolution, not the shape of the latitudinal variation of the eigenfunction. This makes no difference in terms of the computed ratio unless one has the case where a particular mode has undergone an avoided crossing for one mass but not the other. These are rare occurrences. Following the shape in this case changes the frequency ratio for both modes. We show the approximate shift by the cross in Figure 3.5 (right). In terms of increasing rotation rate, the ratios look normal until we reach the rotation rate where the avoided crossing has occurred in one model but not the other. Once the avoided crossing has occurred in both models the ratios look normal again.

Figure 3.6 shows an overview of how the scaling of frequencies look for all masses considered using the eighth most rapid rotating models in our set with velocities around 170 km s^{-1}. It can be seen how the g modes scale differently than the p modes in every case. To give a general idea of how the ratios of the p modes scale for the different mass combinations as well as to see how each ℓ behaves, the average ratio between each acoustic mode with $n > 1$ and the theoretical root-mean density ratio was calculated. Most ratios fall within 0.1% and 1% from the theoretical ratio, where the larger differences correspond to the ratios between models with the biggest mass difference.

3.5 DEPENDENCIES OF THE $\Delta\nu - \sqrt{\bar{\rho}}$

Several studies have been undertaken to examine the utility of the $\Delta\nu - \sqrt{\bar{\rho}}$ relation for δ Scuti variables (e.g., Reese et al. 2008; Suárez et al. 2014; García Hernández et al. 2015). Here $\Delta\nu$ is taken to refer to frequency differences with $\Delta n = 1$ and $\Delta\ell = 0$ for relatively small n instead of in the limit of large n. We discuss the relative importance of three factors that affect this relationship: evolutionary state, rotation, and mass for models with the same rotational shape.

The largest variation in the mean density comes from the evolution of the star along the main sequence, dropping by a little less than a factor of six from the ZAMS to the end of core hydrogen burning for a $2M_\odot$ non-rotating model. In contrast, the change in mean density between our $2M_\odot$ non-rotating model and a $2M_\odot$ model rotating near critical rotation (Deupree 2011a) is less than a factor of two. The change between the mean density of the non-rotating model and the highest rotation rate we consider in this paper is only about 10%. We obtain the same mean density as that for our most rapidly rotating model for an evolved model with $X_c = 0.64$ (the ZAMS models have $X_c = 0.70$). Finally, we

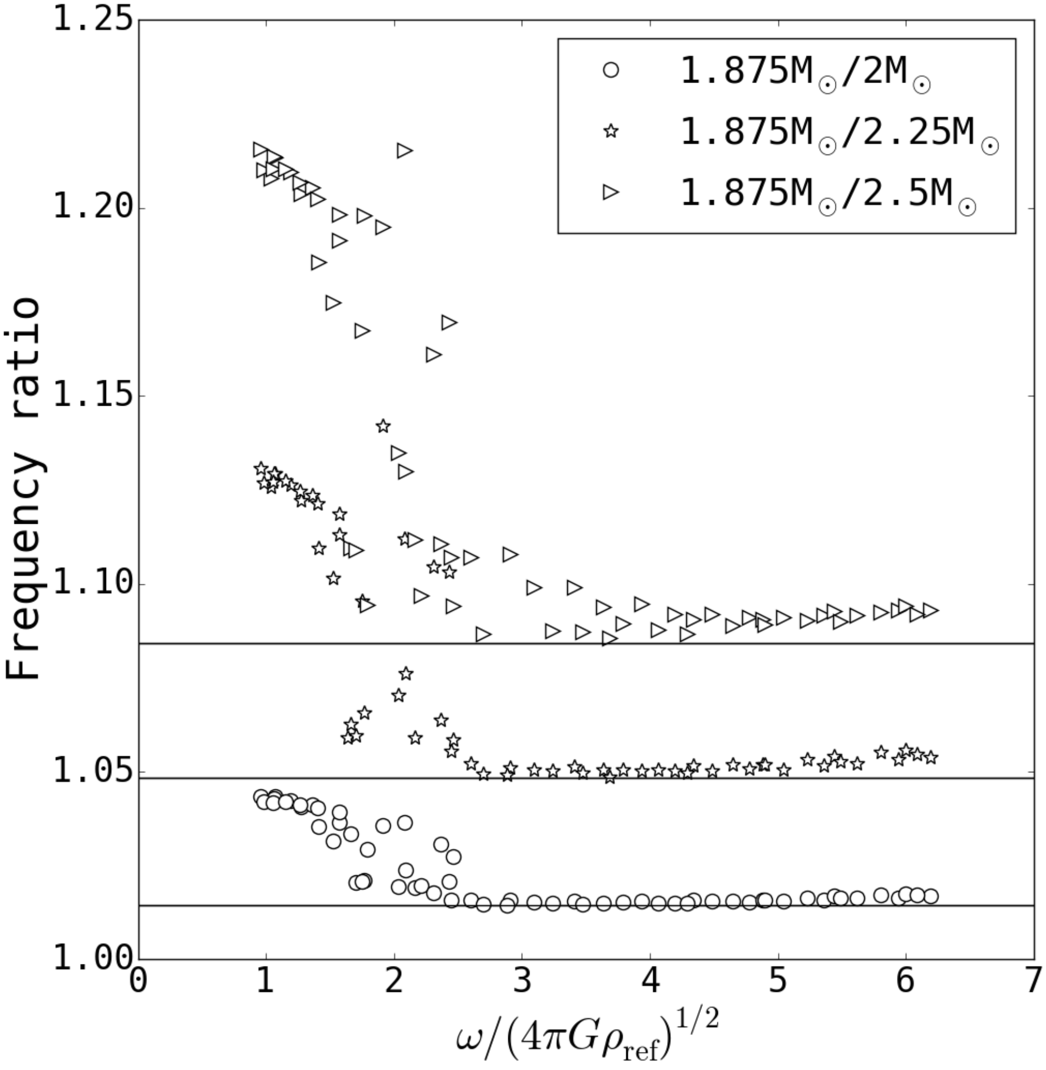

Figure 3.6: General scaling behavior of the frequency ratios between the computed frequencies of the M=1.875$M_\odot$ and the other masses considered for the eighth most rapid rotating models in our set with velocities around 170 km s^{-1}. Modes with ℓ values from 0 through 6 were included. It can be seen how g and p modes scale differently. The horizontal lines correspond to the theoretical ratio of the root-mean density relation for each pair of masses. The p modes fall close to these lines in every case, but depart from the lines progressively more as the relative difference between the two masses increases.

note that the mean density changes by about 17% between our $1.875M_\odot$ and $2.5M_\odot$ ZAMS models (the ratio is the same for all rotation rates because of the way the models were constructed).

We compare the relation between $\Delta\nu$ and $\sqrt{\bar{\rho}}$ as a function of mass for the same evolution state, rotation, and the relation found by García Hernández et al. (2015) and by Suárez et al. (2014) in Figure 3.7. Like Garcia Hernandez et al., we computed $\Delta\nu$ at sufficiently high n so that we could avoid our second frequency region where the p and g modes overlap and the density of modes is comparatively high. This was done by locating the highest frequency mode with g mode characteristics in our most rapidly rotating models and considering the next six modes for each ℓ that can be traced back to modes with $0 \leq \ell \leq 5$ in the non-rotating model. This gives us the modes with $3 \leq n \leq 8$ for which we compute $\Delta\nu$ averaged over the five large separations for each of the six values of ℓ. The modes we use have sufficiently large n that the variation of $\Delta\nu$ with n and ℓ is relatively small in the narrow range we use. We do note that, for lower radial order p modes that we do not include, the power law is nearly the same but the coefficient is different in the relation between the mean density and large separation for different modes.

We find the relation between $\Delta\nu$ and $\sqrt{\bar{\rho}}$ for increasing rotation is very similar to the relation found by Suárez et al. (2014) and García Hernández et al. (2015). In all cases, the slope is very similar to that of the classical period-root mean density relation. The change with mass for the ZAMS models is not as steep, suggesting that the mean density is primarily an indication of evolution stage for models in this range. However, the correlation may not be unique when the results of a rapidly rotating model are compared with those

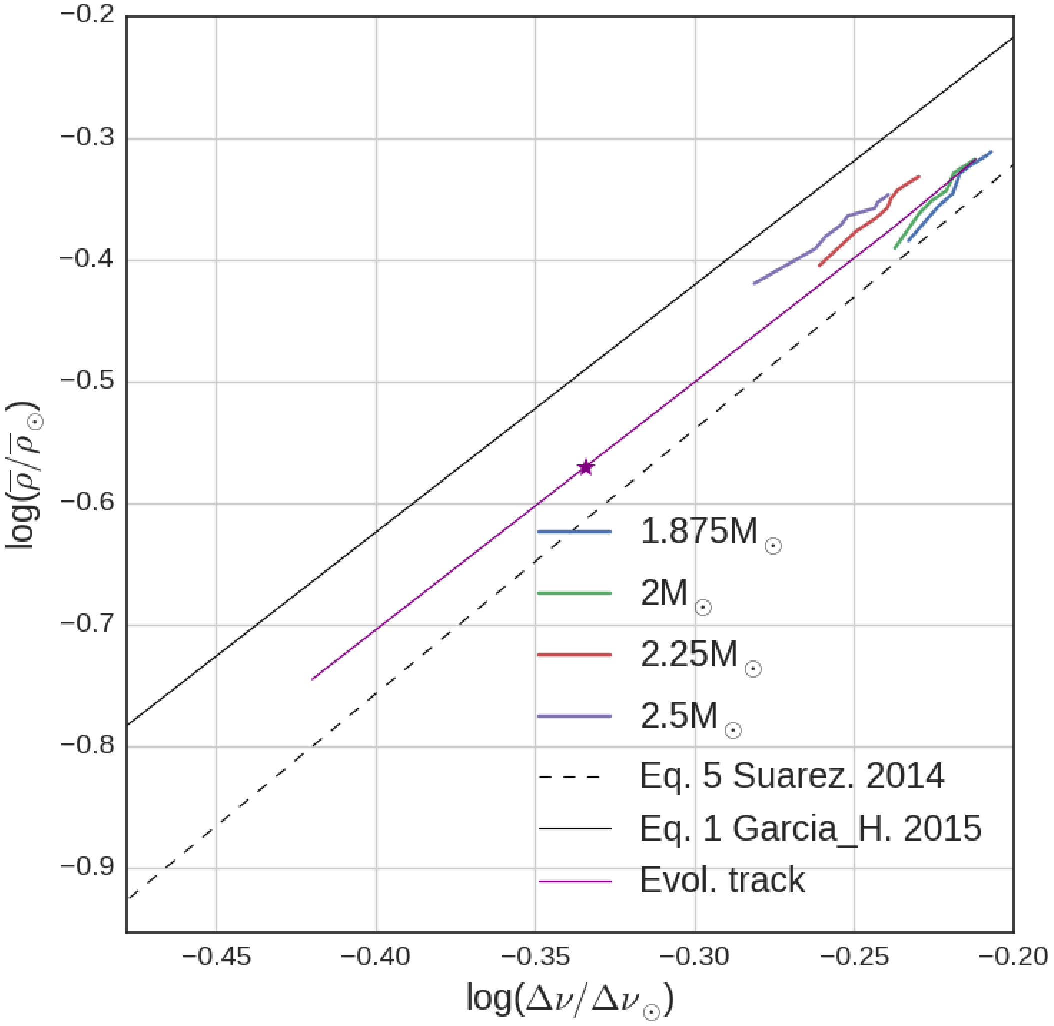

Figure 3.7: Relation between $\Delta\nu$ and $\sqrt{\overline{\rho}}$ for the rotating models considered. Also plotted are the relationships found by previous studies for comparison. The purple line shows how this relationship looks if the non-rotating model with $2M_\odot$ is evolved and the star symbol along this line shows the mean density of a $2M_\odot$ ZAMS model rotating at critical rotation. A colour version of this figure can be found online.

of a slightly evolved non-rotating star, as is shown in Figure 3.7. It goes without saying that obtaining a useful estimate of the mass depends crucially on the quality of the surface radius information.

We have also examined how individual frequencies relate to the mean density. Lovekin et al. (2009) found that a "mean density" computed using values of the surface radius at specific colatitudes gave a nearly linear relationship between the period and mean density when the radius defined at a colatitude of about 40 degrees was used. No particular significance was attached to this result. We have explored this further and agree with Lovekin et al. (2009) for the mode they used, but find that the colatitude required depends on the specific mode being examined. Specifically, we find that either larger n or larger ℓ requires the colatitude for the surface radius to be used in the "mean density" to increase (i.e., the radius must increase). We attach no physical significance to this except as an expression that models with constant mass and evolutionary state but changing rotation do not constitute a homologous family.

3.6 FINAL CONSIDERATIONS

We have examined the variation of both g mode and p mode oscillation frequencies in intermediate mass, uniformly rotating, ZAMS stellar models. The behavior of the p mode frequencies with rotation is similar to that found for a $10_{\odot}$ model by Lovekin & Deupree (2008), suggesting that the behavior will be similar for models with masses in between. By comparing models of different masses with the same surface shape, we found that the period-root mean density relation applies to the p modes for rotating models to the same extent and with the same caveats as it does to non-rotating models.

The g mode frequencies are much less affected by rotation because their frequencies are determined in the region of the model between the convective core boundary and the lower boundary of the second helium ionization region. The region closer to the convective core is probably more important, but the entire region contributes to the frequency determination. For sufficiently low frequencies, the frequency ratio of a given mode for two masses is almost independent of the mode. For these modes there is a slight trend of increasing frequency ratio with decreasing frequency as shown in Figure 3.5.

The most complex region of the frequency spectrum is the region of overlap of the p and g modes. Because the g mode frequencies increase with rotation and the p mode frequencies decrease, the possibility of avoided crossings is high and the frequency ratio for specific modes between two masses may vary significantly as a function of rotation rate. Figure 3.5 suggests that modes with higher latitudinal variation show this feature more strongly than modes with lower latitudinal variation.

Another situation in which the scaling with mass will fail is when a given mode at one mass has undergone an avoided crossing while it has not at the other mass. If the modes rather than the shape of the latitudinal variation can be identified, the scaling holds. Once the mode has undergone the avoided crossings for both masses, the scaling is restored. Despite these problems, the scaling relationships found here should give general guidance on how to alter a model to obtain a better approximation to an observed mode frequency spectrum.

There remains the issue of matching modes observed in stars to modes computed for specific models. We have shown that there are certain scaling relations for the frequencies of a given mode from one model to another which may be helpful as part of this process. However, there are many gaps to fill before we can routinely associate a given observed mode with a specific computed mode. First and foremost is the need to have some reasonable estimate of the inclination of the rotation axis to the observer. If the inclination is low, one might use the shape of the wings of line profiles as for Vega (Gulliver et al. 1991; Takeda et al. 2008; Yoon et al. 2010). Stars with very high observed values of V sin i are presumably seen at high inclinations. Best is the determination of the inclination by optical interferometry, so far restricted to relatively few stars. Even with a reasonably determined inclination, the task is still formidable. An examination of the echelle diagram comparing observed mode frequencies with computed mode frequencies (e.g., Figure 5 of Deupree (2011) for α Oph) provides some indication of how far we have yet to go. Clearly, the density of computed modes requires a windowing process to help us associate an observed mode with a computed mode. For stars with a sizeable number of observed modes, patterns in the observed frequencies may exist for comparison with patterns in the computed frequency spectrum, much as for the Sun. Stars with only a very limited number of modes with sizeable amplitudes may have variations in the colour difference between maximum and minimum light in different filters or variations in the line profiles that could help constrain the possibilities. Similarly, theoretical determination of which modes are pulsationally unstable or otherwise of such low amplitude as to be unobservable at the appropriate inclination would be helpful.

Chapter 4

Exploration of mode observabilities in rapidly rotating stars

4.1 Introduction

The space missions such as MOST (Walker et al. 2003), CoRoT (Baglin et al. 2009), and Kepler (Borucki et al. 2010) have found a large number of intermediate mass stars, a number of which are rapidly rotating, which possess a sizable number of oscillation modes (Poretti et al. 2009; Monnier et al. 2010; Balona et al. 2012). Similarly, linear adiabatic oscillation calculations (e.g., Deupree 2011b; Deupree et al. 2012; Reese et al. 2009, 2013; Ouazzani et al. 2012, 2015) also find a very dense frequency spectrum, particularly if non-axisymmetric modes are included. The density of modes raises the possibility that computed mode frequencies can match observed mode frequencies as much by chance as by a physical match. Attempts to match the observed oscillation spectra of the rapidly rotating delta Scuti star

α Oph obtained by MOST (Monnier et al. 2010) show that there is still no clear way of relating the observed modes with those computed (e.g., Deupree 2011b; Deupree et al. 2012; Mirouh et al. 2013). The echelle diagram comparing observed and computed frequencies (Figure 1 of Deupree et al. 2012) indicates how complex the issue is.

One desirable way to delete computed modes is based on whether they would produce a sufficiently large oscillation amplitude to be observed. Whether or not a particular mode is observable depends on several features – whether the mode is pulsationally unstable or not; if self excited, what determines the limit cycle and, if not, how the mode might be excited; whether there are near resonances in frequency with other modes; and for non-radial modes whether there are significant cancellation effects which reduce the pulsation light variability over the unresolved stellar disk. We note that all of these are relevant, but many cannot be theoretically well addressed currently for non-radial modes. Here we shall focus on the cancellation effects. Because of the exclusion of the other issues mentioned above and even other issues, our comments will necessarily contain the proviso "other things being equal". Nonetheless, very strong cancellation probably does prohibit visibility unless other factors are quite pronounced.

For non-rotating stars, modes with spherical harmonic degrees up to $\ell = 3$ are said to be above the threshold of observation (Dziembowski 1977; Aerts et al. 2010) based on cancellation effects. The issue is more complicated for rapidly rotating models because the oscillations can no longer be modeled as a single spherical harmonic, but rather as a sum of spherical harmonics. Not only does this change the oscillation frequency significantly (Clement 1998; Yoshida & Eriguchi 2001; Espinosa et al. 2004; Lignières et al. 2006; Lovekin

& Deupree 2008; Lovekin et al. 2009; Ouazzani et al. 2012, 2015), but it also changes the latitudinal variation of the perturbations. To obtain accurate oscillation frequencies, one must include a number of spherical harmonics, and the frequency spectrum contains the number of frequencies that correspond to the spectrum of a non-rotating model with all these spherical harmonics included. Including the sum of spherical harmonics in the latitudinal expression of the eigenfunction suggests that the simple prescription for non-rotating stars may not be adequate. Here we wish to determine if a relatively simple replacement can be identified.

Recently, Reese et al. (2013) used linear adiabatic calculations to study the level of observability of modes for rapidly rotating 2 $M_\odot$ models, finding that in general island modes tend to show larger observabilities but that in some geometrical configurations and rotation rates, chaotic modes could potentially be observed. Assuming that the labeling scheme for each mode is associated with the ℓ value of the non-rotating case (done by tracing the mode through a sequence of models with increasing rotational velocities), this essentially means that on most geometrical configurations, modes with low ℓ values still tend to be more likely to be observed than higher ℓ ones.

We also compute the amplitude difference between maximum and minimum light using the adiabatic perturbations. We recognize that non-adiabatic perturbations can be different (e.g., Dupret et al. 2002), but these are the best we have available. Furthermore, our primary interest is in determining how the latitudinal variations of the surface perturbations affect the light amplitude, again with “other things being equal”. In Section 4.2 we discuss how the amplitude differences are obtained. Because the models are rotating, the observed magnitude difference will be a function of the inclination between the viewer and the rotation axis, further complicating what modes will have sizable magnitude differences. Our results are presented in Section 3. A few final comments are provided in Section 4.

4.2 Method of observability calculation

We start with the rotating 2D ZAMS models, both rotating and non-rotating of Deupree (2011a) and oscillation modes of those models computed by Castañeda & Deupree (2016). The 2D models used include nine rotation rates (including zero) for each of three masses between 1.875 and 2.25 $M_{\odot}$. The models are engineered so that the model with the same rotation for each mass is defined by having the same surface shape. The mode perturbations were computed with the linear adiabatic code for rotating models, NRO (Clement 1998) that allows us to write the latitudinal variation of the perturbations as a sum of Legendre polynomials. The perturbations obtained are the Lagrangian displacements, ξ_r and ξ_θ, the Eulerian pressure perturbation, and the Eulerian perturbation of the gravitational potential. Given the constraints of adiabatic calculations, we shall assume that the perturbation of the effective temperature is given by the Lagrangian perturbation of the temperature at the surface. We assume that $\delta T_{\rm eff}/T_{\rm eff} = \delta T/T$ at the appropriate optical depth ($\tau = 2/3$) which, although has been shown to be not necessarily true in non-adiabatic calculations of stellar pulsations (Dupret et al. 2002), should allow a qualitative analysis of whether different modes can be ruled out based on their observability owing to latitudinal cancellations. Denoting Lagrangian perturbations of the state variables by δ and the Eulerian perturbations by a prime, we start with the adiabatic relation between the pressure and temperature, the pressure and density, and the perturbed mass conservation equation:

$$\frac{\delta T}{T} = \frac{\Gamma_3 - 1}{\Gamma_1}\frac{\delta P}{P}, \quad \frac{\delta P}{P} = \Gamma_1 \frac{\delta \rho}{\rho}, \quad \frac{\delta \rho}{\rho} = -\boldsymbol{\nabla} \cdot \boldsymbol{\xi} \tag{4.1}$$

Noting that $\delta P = P' + \boldsymbol{\xi} \cdot \boldsymbol{\nabla P}$, $\boldsymbol{\nabla P} = \rho \boldsymbol{g_{\mathrm{eff}}}$ and defining $p' = P'/\rho - \psi'$, these equations lead to:

$$\boldsymbol{\nabla} \cdot \boldsymbol{\xi} = -\frac{1}{c^2}(p' + \psi' + \boldsymbol{\xi} \cdot \boldsymbol{g_{\mathrm{eff}}}) \tag{4.2}$$

where c is the adiabatic speed of sound, given by $\sqrt{\Gamma_1 P/\rho}$. Once we have $\boldsymbol{\nabla} \cdot \boldsymbol{\xi}$, we can solve for the horizontal perturbations of the temperature using equation 4.1. Of course, we have another expression for $\boldsymbol{\nabla} \cdot \boldsymbol{\xi}$, given by (assuming axisymmetric modes):

$$\boldsymbol{\nabla} \cdot \boldsymbol{\xi} = \frac{1}{r^2}\frac{\partial}{\partial r}(r^2 \xi_r) + \frac{1}{r\,\mathrm{sin}\theta}\frac{\partial}{\partial \theta}(\xi_\theta\,\mathrm{sin}\theta) \tag{4.3}$$

which was used to check for consistency in our temperature perturbation calculations. We also compared our calculations of $\boldsymbol{\nabla} \cdot \boldsymbol{\xi}$ with those found Guenther's non-radial stellar pulsation code (Guenther 1994) for a non-rotating model. The verification was required because the NRO code makes several variable transformations and we needed to be sure that we had performed the inverse transformations properly. The Lagrangian nature of the displacement perturbations and non-zero values of ξ_θ cause the Lagrangian temperature perturbations to be defined at new latitudinal locations.. We obtain the perturbation values at the original latitude points by interpolating these perturbations using a sum of eight Legendre polynomials (the same number of Legendre polynomials used in computing the pulsation modes themselves).

Finally, we set the maximum radial perturbation to some value (∼1% of the radius of the star) and scaled all perturbed quantities by the same amount. Finally, the perturbations and the static model 2D surface properties are separately interpolated onto a grid of 200 latitudinal points by 400 azimuthal points and then added together.

We computed the SED of each perturbed model at maximum and minimum light at each of ten inclinations uniformly spaced between 0 and 90 degrees. The SED calculation was done by computing the weighted integral of the intensity integrated over the visible surface of the star. Such integration has been used in various other studies (e.g., Slettebak et al. 1980; Linnell & Hubeny 1994; Frémat et al. 2005; Gillich et al. 2008; Aufdenberg et al. 2006; Yoon et al. 2008; Dall & Sbordone 2011; Deupree et al. 2012). The set of emergent intensities used in the weighted integral was obtained from NLTE plane parallel atmospheres computed with the PHOENIX code (Hauschildt & Baron 1999). The specific details on both the PHOENIX calculations and the calculation of the SEDs are found in Lovekin et al. (2006) and Gillich et al. (2008). With the computed SEDs we performed photometric calculations for the Walraven (Walraven & Walraven 1960) and Johnson (Johnson et al. 1966) filter systems. For simplicity we present the results based on the calculated magnitudes in the Walraven u band, noting that we have obtained similar results in the other filters. The magnitude difference between the filtered SEDs at maximum and minimum light provide the measurement we will use to determine the mode's observability.

4.3 Results

We first examine the amplitude variation with respect to ℓ for a given radial node identifier n and rotation rate. Here the arbitrary scaling of the modes poses no difficulty - all modes are scaled by the same amount because they apply to the same model. Again, this should provide the relative pulsation amplitudes (we shall refer to these hereinafter as "observabilities") as long as all modes have the same excitation, non-adiabatic and possibly other effects. We present the surface radial perturbation as a function of colatitude for $n = 5$ for values of ℓ between 0 and 5 in Figure 4.1. These are pure Legendre polynomials because the rotational velocity is zero. The associated observabilities of these modes are shown in Figure 4.2 as functions of inclination. As expected, the observability decreases with increasing ℓ except at inclinations where nodes in the perturbation play a significant role.

The picture for a more rapidly rotating model is somewhat more complex. Here, and in subsequent discussion, the value of ℓ assigned is obtained by tracking the mode through the rotation sequence back to zero rotation. Of course, this label is merely one of convenience rather than a designation of an actual ℓ. Figure 4.3 shows the latitudinal variation of the surface radial perturbation as a function of colatitude. Only the $\ell = 5$ mode has approximately the same latitudinal shape as that mode for the non-rotating model. Figure 4.4 shows the corresponding observabilities of these modes. The $\ell = 0$ mode has the highest observability when seen pole on, although the amount is much smaller than in the non-rotating case, while the $\ell = 2$ and $\ell = 4$ modes are now more observable than the other modes when seen equator on.

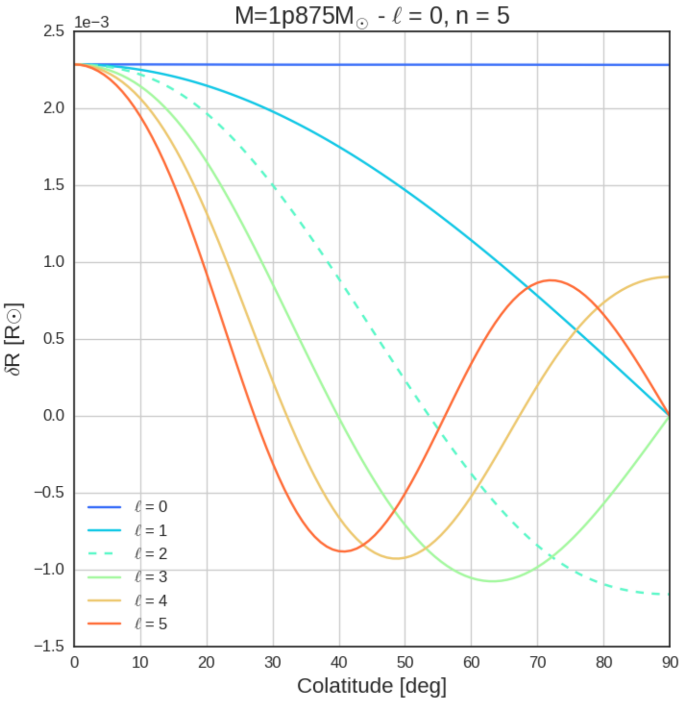

Figure 4.1: The surface radial perturbation as a function of colatitude for $n = 5$ for values of ℓ between 0 and 5 for a non-rotating, M=1.875M$_\odot$ model.

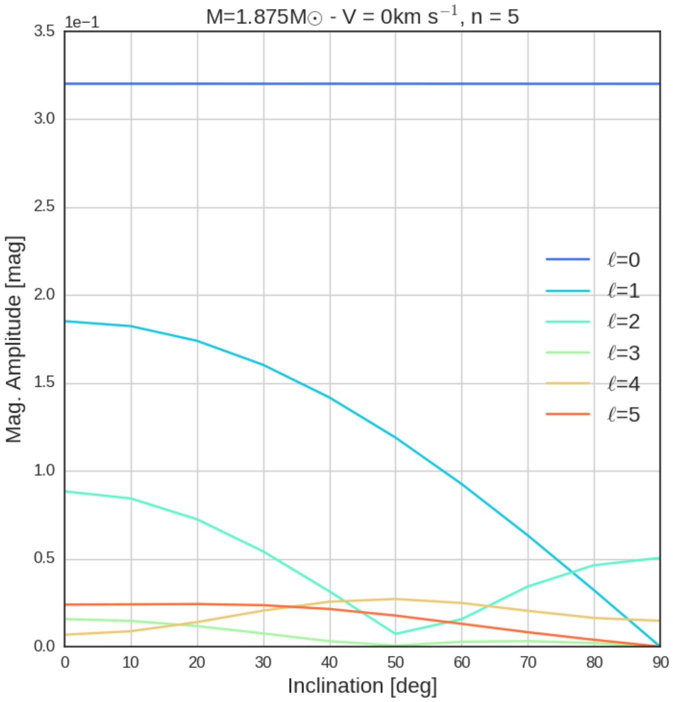

Figure 4.2: Magnitude amplitude as a function of colatitude for $n = 5$ for values of ℓ between 0 and 5 for the non-rotating case.

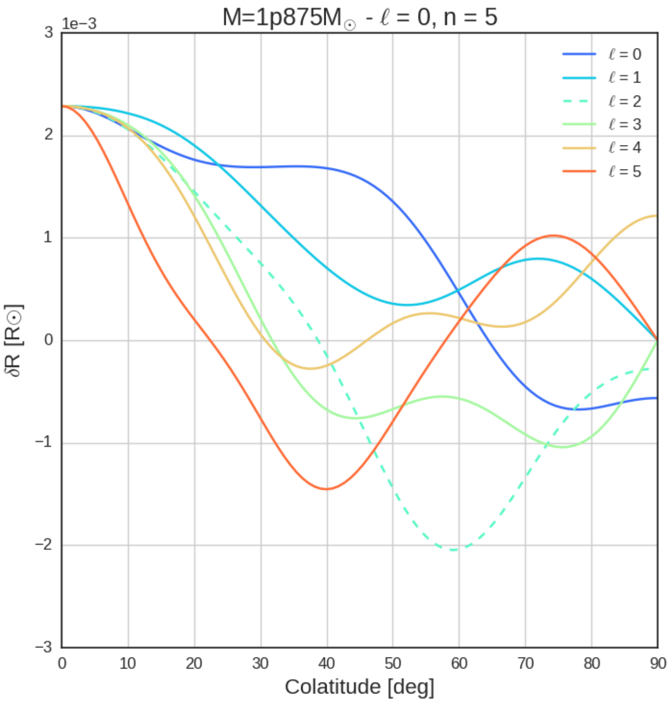

Figure 4.3: The surface radial perturbation as a function of colatitude for $n = 5$ for values of ℓ between 0 and 5 for a M=1.875M$_\odot$ model with equatorial velocity of 187 km s^{-1}. Note the differences in the radial perturbations from those in Figure 4.1.

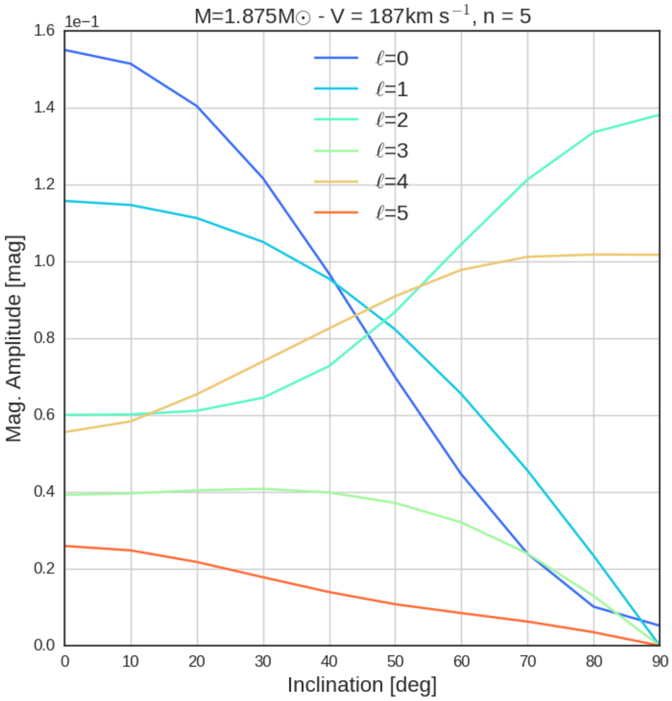

Figure 4.4: Magnitude amplitude as a function of colatitude for $n = 5$ for values of ℓ between 0 and 5 for a M=1.875M$_\odot$ model with equatorial velocity of 187 km s^{-1}. The values of ℓ for the individual modes are obtained by following specific modes through a sequence of models of increasing rotation from the non-rotating model to the current one. Note the difference in amplitude scale between this figure and Figure 4.2, and note the differences between the pulsation amplitudes between the ones presented here and in Figure 4.2.

In order to compare the same mode at different rotation rates, we must determine how to scale the mode for each model. We first attempted scaling so that each model in a rotation sequence had the same relative radial perturbation at the pole, the logic being that the polar radius does not change appreciably as the rotation rate increases. However, this amplified the observability of those modes which had a modest perturbation at the pole compared to other latitudes. The effect becomes more prominent as increasing rotation tends to focus the larger amplitude radial perturbations towards the equator (e.g., Clement 1998; Lignières et al. 2006; Reese et al. 2013). We then decided to determine the perturbation scaling by requiring that the maximum value of δr be the same for each model of the rotation sequence, regardless of the inclination at which it occurs. While not rigorous, this scaling approach should give us an estimate of the relative observability as a function of rotation rate.

Perhaps the most interesting results are for the nominally radial modes. We show the variation of the radial perturbation with colatitude for $n = 5$ in Figure 4.5. Here we see that only a very small amount of rotation is required for the mode to become noticeably aspherical. At a rotation rate of only about 105 km s^{-1} the radial mode more closely resembles an $\ell = 1$ mode more than anything else.

Higher rotation rates produce a high colatitude node which moves toward mid latitudes as the rotation rate increases. Thus, the mode begins to show something of an $\ell = 2$ appearance. We point out that this is very similar to the behavior of the radial mode computed for a 10 $M_\odot$ model by Lovekin & Deupree (2008). However, it should also be noted that, while the evolution of the radial mode latitudinal profile is similar for each positive value of n examined, a given radial perturbation latitudinal profile requires a larger rotational velocity at lower values of n. For example, a velocity of about 146 km s^{-1} is needed to produce the same effect for the 2H mode that a velocity of 62 km s^{-1} produces in the 5H mode. We show how the evolution in radial perturbation changes the observability in Figure 4.6, a plot of the amplitude versus inclination for the different rotation rates. The chief effect is the substantial decrease in amplitude at all inclinations. Also significant is the fact that the decrease is appreciably larger when seen equator on compared to when seen pole on. This is the result of the transition of the modes being described by $\ell = 0$ at low rotation to something more closely resembling $\ell = 1$ at higher rotation.

The decrease in change of radial perturbation with decreasing n for the radial modes is maintained down to $n = 1$. The radial fundamental mode is different, with the radial perturbation decreasing at the pole with increasing rotation rather than at the equator. We show the variation of the radial perturbation of the radial fundamental mode with colatitude for various rotation rates in Figure 4.7. There is a resonance (the frequency difference is about 0.05%) for V = 62 km s^{-1} with a $\ell = 4$ g-mode. The pulsation amplitude is shown in Figure 4.8. We see that the pulsation amplitude for this rotation rate is reduced to compared to where it would otherwise be, but the pulsation amplitude profiles are similar to those of the radial harmonic modes except for the reversal of latitude. Looked at as a combination of Legendre polynomials, we note that the $\ell = 0$ and $\ell = 2$ contributions have the same sign for $n > 0$, but different signs for $n = 0$. We note that we cannot compare the pulsation amplitudes for p modes with different n because the radial derivative of the radial perturbation becomes steeper as n increases, and hence $\boldsymbol{\nabla} \cdot \boldsymbol{\xi}$ becomes larger. Given the relations in the previous section, the relative temperature perturbations become larger

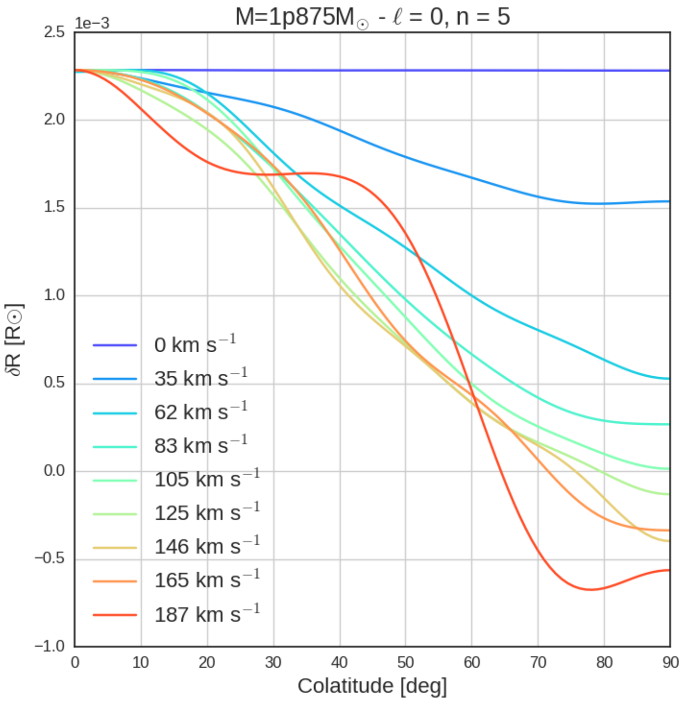

Figure 4.5: The surface radial perturbation as a function of colatitude for $n = 5$, $\ell = 0$ for various rotation rates of a M=1.875M$_\odot$ model.

as well, increasing the pulsation amplitude.

Another interesting case is the change in the radial perturbation of the $\ell = 1$, $n = 5$ mode, shown in Figure 4.9. Here the change in the radial perturbation is relatively modest until a rotation rate of 146 km s^{-1} is reached. This produces a wave in the perturbation, but the latitudinal profile of the radial perturbation at the 165 km s^{-1} rotation rate is completely different. This is because the $\ell = 1$ mode has a near resonance (a 0.15% frequency difference between the two modes) with an $\ell = 11$ mode.

The effect of this near degeneracy on the observability is shown in Figure 4.10, a plot of the amplitude versus the inclination for this mode at all rotation rates. The trend toward

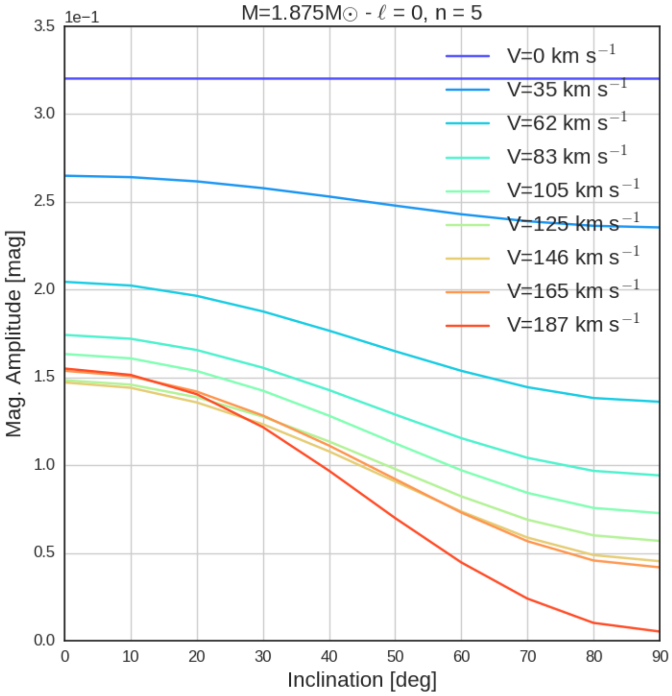

Figure 4.6: The magnitude amplitudes as a function of inclination for $n = 5$, $\ell = 0$ for various rotation rates of a M=1.875M$_\odot$ model.

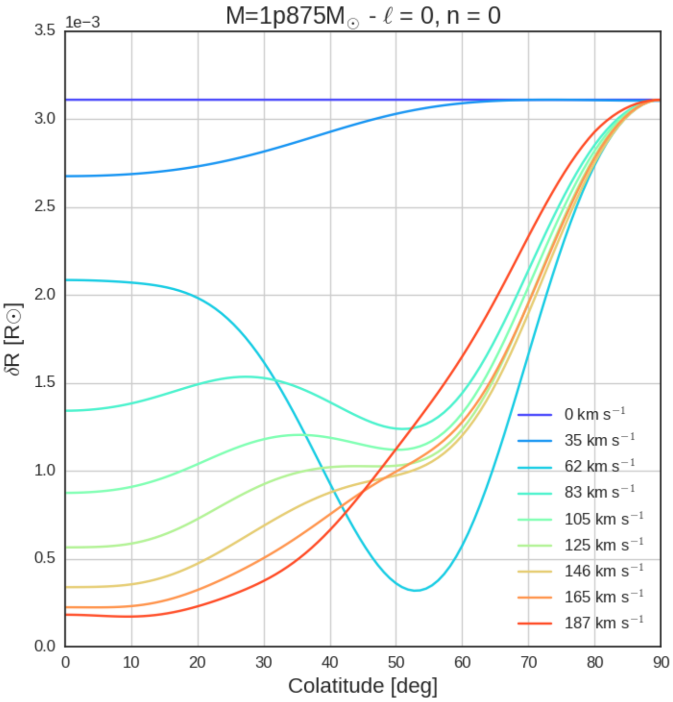

Figure 4.7: The surface radial perturbation as a function of colatitude for the radial fundamental mode for various rotation rates of a M=1.875M$_\odot$ model.

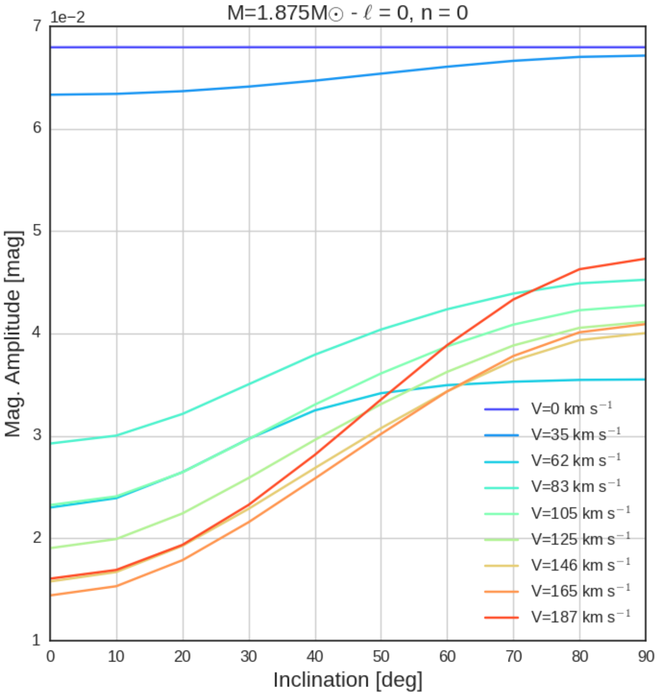

Figure 4.8: The magnitude amplitudes as a function of inclination for the radial fundamental mode for various rotation rates of a M=1.875M$_\odot$ model.

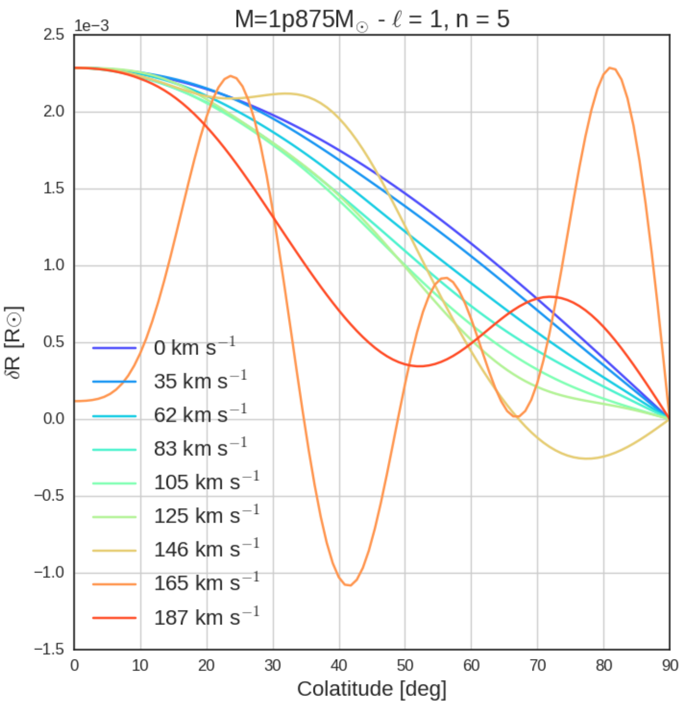

Figure 4.9: The surface radial perturbation as a function of colatitude for $n = 5$, $\ell = 1$ for various rotation rates of a M=1.875M$_\odot$ model. Note the change of the radial perturbation at the 165 km s^{-1} rotation rate caused by a resonance with an $\ell = 11$ mode.

lower amplitudes at all inclinations is apparent, but we note that the pulsation amplitude for the 165 km s^{-1} is much lower than all the others, including the 187 km s^{-1} case.

We have also compared the observability calculations for models with masses of 2 and 2.25 M$_\odot$. The trends in both masses are the same as shown here for 1.875 M$_\odot$, including the behavior of the radial modes. A comparison of the radial perturbations for $\ell = 1$, $n = 5$ may be seen by a comparison of Figure 4.9 with Figure 4.11. The major differences are tied to resonances. The same resonances occur for all masses, but they occur at slightly different rotation rates for each mass. The pulsation magnitudes are also quite similar except for

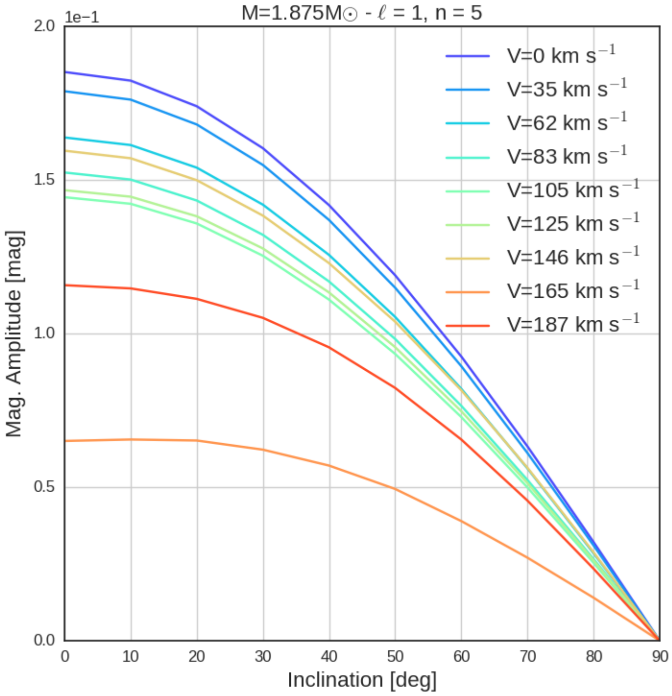

Figure 4.10: The magnitude amplitudes as a function of inclination for $n = 5$, $\ell = 1$ for various rotation rates of a M=1.875M$_\odot$ model. Due to the resonance with the $\ell = 11$ mode at 165 km s^{-1}, the magnitude amplitude is reduced compared to those at both higher and lower rotation rates.

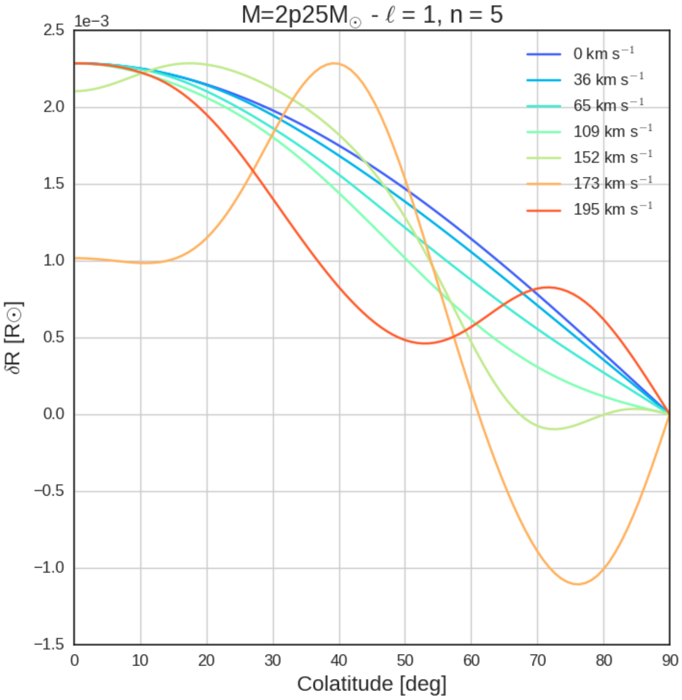

Figure 4.11: The surface radial perturbation as a function of colatitude for $n = 5$, $\ell = 1$ for various rotation rates of a M=2.25M$_\odot$ model. Note the differences between the resonance found at 173 km s^{-1} with the one found at 165 km s^{-1} for the model with mass of 1.875M$_\odot$ in Figure 4.9.

those cases affected by resonances.

We have computed the pulsation amplitudes for all modes with $\ell < 11$ and $n = 5$ for all rotation rates. These are presented in Figures 4.12, 4.13, and 4.14 for inclinations of 10, 40, and 80 degrees, respectively. We see that, with very few exceptions, the amplitudes of the modes with $\ell > 5$ (given by the dashed lines in the figures), are all smaller than those of lower ℓ. Spikes upward or downward in these plots usually represent resonances, such as for $\ell = 1$, $i = 10^\circ$, and $(V_{\rm eq}/V_{\rm ref})^2 = 2.7$. The modes at $i = 10^\circ$ more or less keep their same order as the rotation rate increases, and there is usually some noticeable difference in

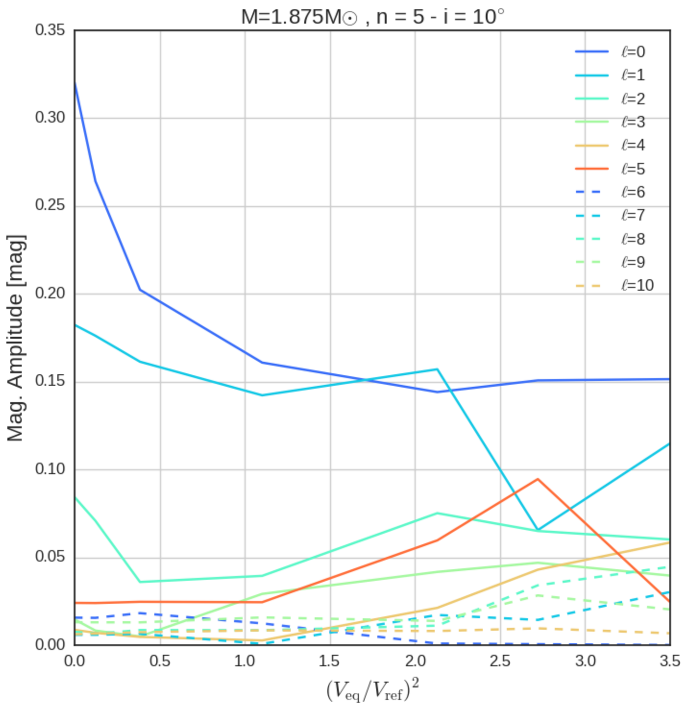

Figure 4.12: The magnitude amplitudes of ℓ values between 0 and 10 for an inclination angle of 10° as a function of rotation rate of a M=1.875M$_\odot$ model. The rotational velocities are scaled by $V_{\rm ref} = 100$ km s^{-1}.

amplitude from one to the next. This is not true in the $i = 40°$ case, where at intermediate rotation the $\ell = 0$, 1, and 2 modes tend to clump together, as do $\ell = 3$, 4, and 5. As one might expect, the even ℓ modes dominate at $i = 80°$ because the radial perturbations of the odd modes vanish at the equator. The $\ell = 0$ mode, which from Figure 4.5 is seen to resemble an $\ell = 1$ mode, also has a much lower amplitude. The $\ell = 2$ and 4 modes have the highest pulsation amplitudes.

These results suggest that one may be able to ignore modes described as $\ell > 5$ at all rotation values considered here unless the pulsation amplitude of the observed mode is very

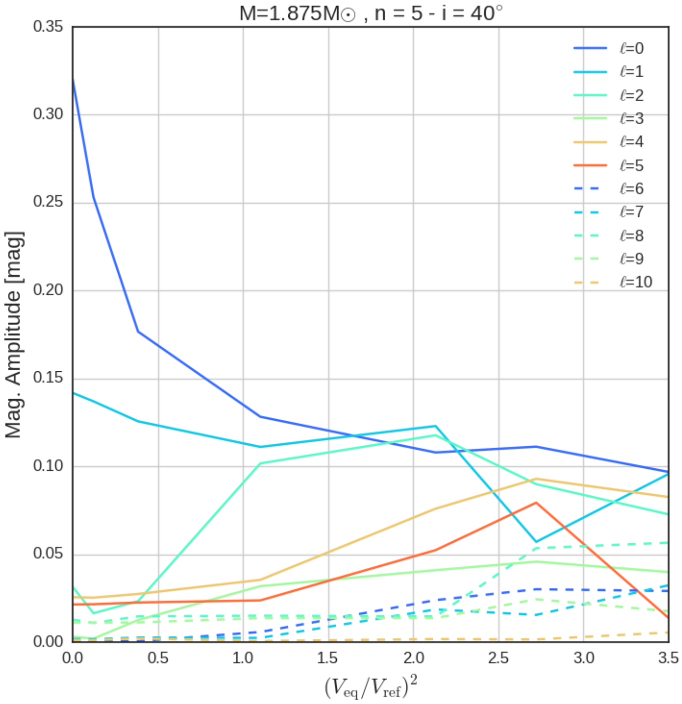

Figure 4.13: The magnitude amplitudes of ℓ values between 0 and 10 for an inclination angle of 40° as a function of rotation rate of a M=1.875M$_\odot$ model. The rotational velocities are scaled by $V_{\rm ref} = 100$ km s^{-1}.

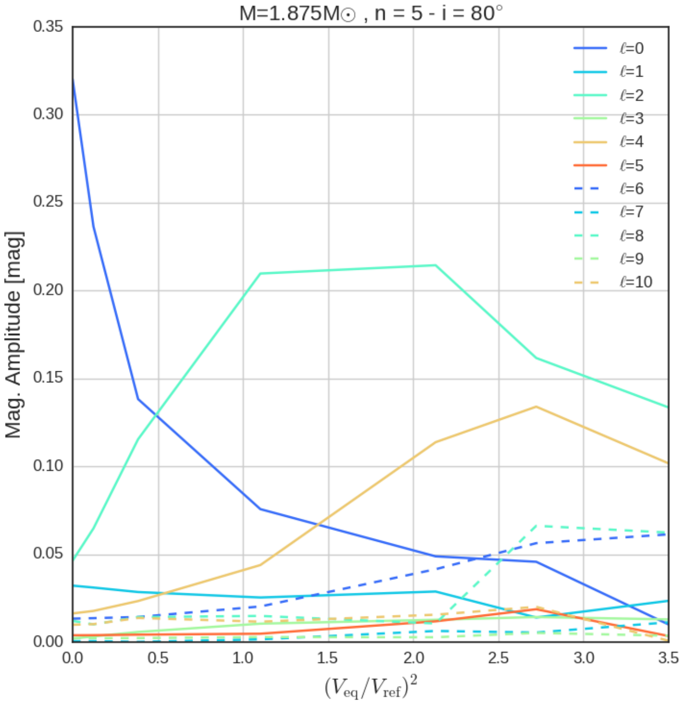

Figure 4.14: The magnitude amplitudes of ℓ values between 0 and 10 for an inclination angle of 80° as a function of rotation rate of a M=1.875M$_\odot$ model. The rotational velocities are scaled by $V_{\rm ref} = 100$ km s^{-1}.

small. Possible exceptions certainly include resonances and may include higher order even modes when seen equator on.

The g-modes in these models are affected far less than the p-modes by rotation, They have comparatively large amplitude exterior to the convective core, deep in the model where the rotational effects are significantly less than near the surface. Larger ℓ modes at a given n appear to be more affected by rotation than smaller ℓ's, both in terms of the radial perturbation and the pulsation amplitude. Higher radial order g-modes appear to be progressively affected less by rotation. Furthermore, the lower radial order, higher ℓ g-modes are in the relatively dense frequency regime which includes not only g-modes, but also p-modes and mixed modes. The possibilities for resonances are thus not terribly small at higher rotation rates. We show the radial perturbation and the pulsation amplitude in Figures 4.15 and 4.16 for a typical g-mode. All of the g-mode amplitudes are small using the same δr as for the p-modes. We note that the latitudinal motion is more significant in the g-modes than the p-modes for a given radial variation, and, while this has been included in the calculations, it needs to be addressed more fully in a future analysis.

4.4 Final Comments

We have computed oscillation mode observabilities for a number of masses, n, ℓ, and rotation rates. The results suggest that, while one may safely remove high ℓ modes from consideration in matching observed modes because of cancellation effects, there will be exceptions. We have also shown that the effects of mass are relatively modest, as long as

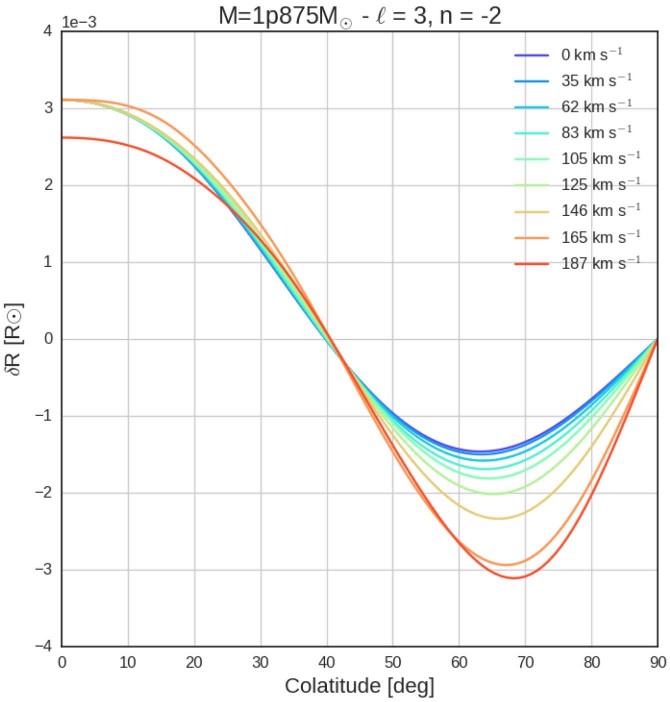

Figure 4.15: The surface radial perturbation as a function of colatitude for n = -2, $\ell = 3$ for various rotation rates of a M=1.875M$_\odot$ model.

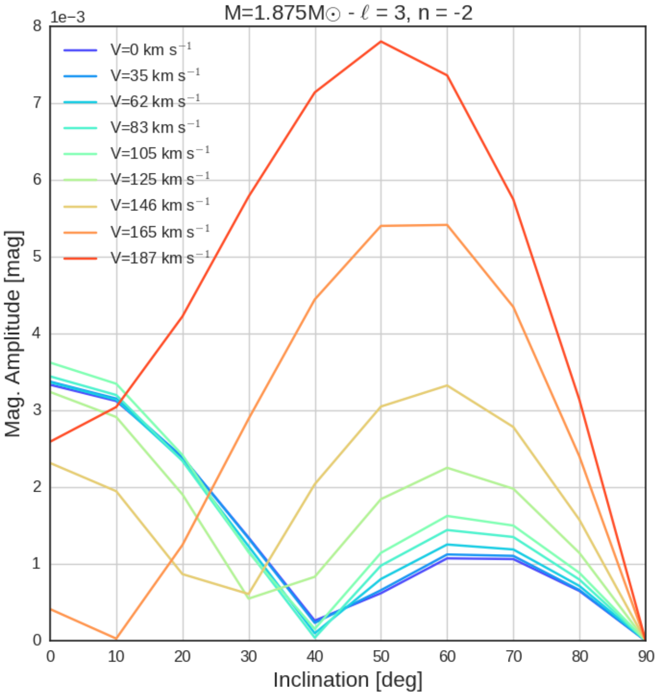

Figure 4.16: The magnitude amplitudes as a function of inclination for n = -2, ℓ = 3 for various rotation rates of a M=1.875M$_\odot$ model.

the mode comparison between two masses was performed on models which have the same surface shape (using this as the indicator of the rotation rate). The radial p modes seem to be more affected than the other ℓ modes, at least for $1 <= n <= 7$. The radial fundamental mode is also affected, but the decrease in pulsation amplitude occurs in the polar regions instead of the equatorial regions like for the other values of n. Finally, we note the role of near resonances in frequency between two modes which can make a given mode either more or less likely to be observable.

Chapter 5

Conclusions

Modeling an individual rotating star can be a very complicated and tedious process using the traditional observational and theoretical tools available. In this thesis we have introduced a set of scaling relationships for observable properties and asteroseismic frequencies found for uniformly rotating ZAMS models that have the same surface shape due to rotation. We have also shown that when only linear adiabatic oscillation calculations are available, it might be possible to exclude calculated modes from the comparison between the calculated oscillation spectra of a rotating star with the observed oscillation spectra of a particular rotating star. The three components of the thesis could be combined to match the observed properties of a rapidly rotating star. In this chapter we will provide a possible example of how they might be applied.

Assume that we have a rotating star where the oblateness, inclination, SED, v sin i, distance, reddening, and mode frequencies are known. We first need to determine where in the HR diagram the rotating star should be placed. We can start by applying the scaling relations from chapter 2 to the observed star and a ZAMS star with a rotation rate that produces the same surface shape. This provides all the surface properties, especially $T_{\rm eff}$ and $g_{\rm eff}$ as functions of latitude. With these known, one can compute the SED for comparison with the observed SED. If necessary, the scaling relationships can be further employed to obtain a better fit to the SED. At the end of this process we have good estimates for the actual luminosity and effective temperature.

The next step is to obtain a rotating model which meets the actual luminosity, effective temperature, and surface shape. This can be done with ROTORC evolution from the ZAMS or from a sequence of rotating evolved models, should they be available. A close model can be modified to change its radius and rotation rate, keeping the same composition profile, to better match the observed conditions.

Assuming the model is now quite close matching observed the spectral properties, the oscillation frequency spectrum can be calculated. It is unlikely that the computed mode frequencies will be a match to the observed ones, but changing the model slightly may bring the observed and computed frequencies into reasonably close agreement. Using the scaling relationships described in Chapter 3 of this thesis, one could understand how the model needs to be changed in order to find a better agreement with the observed oscillation frequencies. For example, if there is a good agreement between the high frequency p modes but not with the low frequency g modes, this might suggest that the conditions near the core of the model used are not similar to the properties in the same region inside of the star observed.

Finally, for non-rotating models modes with $\ell > 3$ are usually omitted from consideration when comparing individual modes calculated with those observed from a star, but the picture is not as clear for rotating models. One way to express the latitudinal variation of the oscillation perturbations for rotating models is with a sum of Legendre polynomials instead of just a single one, so the criterion for omitting modes is a little more complex. We have chosen one based on cancellation effects, although we recognize this is not the only consideration. The results from Chapter 4 suggest that depending of the inclination and rotation rate, we could eliminate a sizable number of computed modes from consideration. In the event that we find a model which matches the observed modes to a certain extent, we can use the procedure in Chapter 4 to eliminate a number of computed modes as prospective matches based on the mode observability, perhaps making a stronger case that remaining modes which match observed ones do not do so by coincidence.

Currently the number of rotating stars for which there are both interferometric and space based asteroseismic observations is limited to α Oph but there is a growing list of interferometric targets (see Table 4 in van Belle 2012) that contains rotating stars that might be expected to show pulsational properties. It would be of great interest to coordinate an effort to study the observed oscillation spectra and apply the ideas explored in this thesis to model more individual stars.

Bibliography

Abt, H. A. & Morrell, N. I. 1995, The Astrophysical Journal Supplement Series, 99, 135

Aerts, C., Christensen-Dalsgaard, J., & Kurtz, D. W. 2010, Asteroseismology

Aufdenberg, J. P., Merand, A., du Foresto, V. C., et al. 2006, ApJ , 645, 664

Baglin, A., Auvergne, M., Barge, P., et al. 2009, in IAU Symposium, Vol. 253, Transiting Planets, ed. F. Pont, D. Sasselov, & M. J. Holman, 71–81

Baglin, A., Auvergne, M., Catala, C., Michel, E., & COROT Team. 2001, in ESA Special Publication, Vol. 464, SOHO 10/GONG 2000 Workshop: Helio- and Asteroseismology at the Dawn of the Millennium, ed. A. Wilson & P. L. Pallé, 395–398

Ballot, J., Lignières, F., Prat, V., Reese, D. R., & Rieutord, M. 2012, in Astronomical Society of the Pacific Conference Series, Vol. 462, Progress in Solar/Stellar Physics with Helio- and Asteroseismology, ed. H. Shibahashi, M. Takata, & A. E. Lynas-Gray, 389

Ballot, J., Lignières, F., Reese, D. R., & Rieutord, M. 2010, A&A , 518, A30

Balona, L. A., Breger, M., Catanzaro, G., et al. 2012, MNRAS , 424, 1187

Basri, G., Borucki, W. J., & Koch, D. 2005, New Astron. Rev., 49, 478

Bernacca, P. L. & Perinotto, M. 1970, Contr. Oss. Astrof. Padova in Asiago

Bessell, M. S., Castelli, F., & Plez, B. 1998, A&A

Borucki, W. J., Koch, D., Basri, G., et al. 2010, Science, 327, 977

Breger, M. 2000, in Astronomical Society of the Pacific Conference Series, Vol. 210, Delta Scuti and Related Stars, ed. M. Breger & M. Montgomery, 3

Castañeda, D. & Deupree, R. G. 2014, ApJ , 794, 13

Castañeda, D. & Deupree, R. G. 2016, MNRAS , 458, 4422

Castelli, F. & Kurucz, R. L. 1994, A&A, 281, 817

Che, X., Monnier, J. D., Zhao, M., et al. 2011, The Astrophysical Journal, 732, 68

Claret, A. 2012, A&A , 541, A113

Claret, A. 2016, A&A , 588, A15

Clement, M. J. 1998, ApJS , 116, 57

Collins, II, G. W. & Smith, R. C. 1985, MNRAS , 213, 519

Collins, George W., I. & Harrington, J. P. 1966, ApJ, 146, 152

Cowling, T. G. & Newing, R. A. 1949, ApJ , 109, 149

Cunha, M. S., Aerts, C., Christensen-Dalsgaard, J., et al. 2007, A&A Rev. , 14, 217

Dall, T. H. & Sbordone, L. 2011, Journal of Physics Conference Series, 328, 012016

Deupree, R. G. 1990, ApJ , 357, 175

Deupree, R. G. 1995, ApJ , 439, 357

Deupree, R. G. 2011a, ApJ , 735, 69

Deupree, R. G. 2011b, ApJ , 742, 9

Deupree, R. G. 2011, ApJ , 742, 9

Deupree, R. G. & Beslin, W. 2010, ApJ , 721, 1900

Deupree, R. G., Castañeda, D., Peña, F., & Short, C. I. 2012, ApJ , 753, 20

Dintrans, B. & Rieutord, M. 2000, A&A , 354, 86

Domiciano de Souza, A., Kervella, P., Jankov, S., et al. 2003, A&A , 407, L47

Dupret, M.-A., De Ridder, J., Neuforge, C., Aerts, C., & Scuflaire, R. 2002, A&A , 385, 563

Dziembowski, W. 1977, **??**jnlActa Astron., 27, 203

Dziembowski, W. A. & Goode, P. R. 1992, ApJ , 394, 670

Elvey, C. T. 1930, ApJ , 71

Endal, A. S. & Sofia, S. 1976, The Astrophysical Journal, 210, 184

Endal, A. S. & Sofia, S. 1978, The Astrophysical Journal, 220, 279

Espinosa, F., Pérez Hernández, F., & Roca Cortés, T. 2004, in ESA Special Publication, Vol. 559, SOHO 14 Helio- and Asteroseismology: Towards a Golden Future, ed. D. Danesy, 424

Espinosa Lara, F. & Rieutord, M. 2011, A&A , 533, A43

Faulkner, J., Roxburgh, I. W., & Strittmatter, P. A. 1968, The Astrophysical Journal, 151, 203

Frémat, Y., Zorec, J., Hubert, A.-M., & Floquet, M. 2005, A&A , 440, 305

García Hernández, A., Martín-Ruiz, S., Monteiro, M. J. P. F. G., et al. 2015, ApJ , 811, L29

García Hernández, A., Moya, A., Michel, E., et al. 2013, A&A , 559, A63

Gillich, A., Deupree, R. G., Lovekin, C. C., Short, C. I., & Toqué, N. 2008, ApJ , 683, 441

Guenther, D. B. 1994, ApJ , 422, 400

Gulliver, A. F., Adelman, S. J., Cowley, C. R., & Fletcher, J. M. 1991, The Astrophysical Journal, 380, 223

Hadjara, M., Domiciano de Souza, A., Vakili, F., et al. 2014, A&A , 569, A45

Hardorp, J. & Strittmatter, P. A. 1968, ApJ, 151, 1057

Hauschildt, P. H. & Baron, E. 1999, J. Comput. Appl. Math., 109

Hayes, D. S. & Latham, D. W. 1975, ApJ, 197, 593

Jackson, S. 1970, The Astrophysical Journal, 161, 579

Jackson, S., MacGregor, K. B., & Skumanich, A. 2004, The Astrophysical Journal, 606, 1196

Jackson, S., MacGregor, K. B., & Skumanich, A. 2005, The Astrophysical Journal Supplement Series, 156, 245

Johnson, H. L., Mitchell, R. I., Iriarte, B., & Wisniewski, W. Z. 1966, Communications of the Lunar and Planetary Laboratory, 4

Kippenhahn, R. & Thomas, H. 1970, Stellar Rotation

Kjeldsen, H., Christensen-Dalsgaard, J., Handberg, R., et al. 2010, Astron. Nachrichten, 331, 966

Ledoux, P. 1949, Memoires of the Societe Royale des Sciences de Liege, 9, 3

Lee, U. & Saio, H. 1986, MNRAS , 221, 365

Lee, U. & Saio, H. 1997, ApJ , 491, 839

Lignières, F. & Georgeot, B. 2009, A&A , 500, 1173

Lignières, F., Rieutord, M., & Reese, D. 2006, A&A , 455, 607

Linnell, A. P. & Hubeny, I. 1994, ApJ , 434, 738

Lovekin, C. C. & Deupree, R. G. 2008, ApJ , 679, 1499

Lovekin, C. C., Deupree, R. G., & Clement, M. J. 2009, ApJ , 693, 677

Lovekin, C. C., Deupree, R. G., & Short, C. I. 2006, ApJ , 643, 460

MacGregor, K. B., Jackson, S., Skumanich, A., & Metcalfe, T. S. 2007, The Astrophysical Journal, 663, 560

Maeder, A. & Peytremann, E. 1970, Astronomy and Astrophysics, 7, 120

Michel, E., Baglin, A., Weiss, W. W., et al. 2008, Communications in Asteroseismology, 156, 73

Mirouh, G. M., Reese, D. R., Lara, F. E., Ballot, & Rieutord, M. 2013, Proceedings of the International Astronomical Union, 9, 455

Monaghan, F. F. & Roxburgh, I. W. 1965, Monthly Notices of the Royal Astronomical Society, 131

Monnier, J. D., Townsend, R. H. D., Che, X., et al. 2010, ApJ , 725, 1192

Monnier, J. D., Zhao, M., Pedretti, E., et al. 2007, Science, 317, 342

Osaki, J. 1975, PASJ , 27, 237

Ostriker, J. P. & Mark, J. W.-K. 1968, The Astrophysical Journal, 151, 1075

Ouazzani, R.-M., Dupret, M.-A., & Reese, D. R. 2012, A&A , 547, A75

Ouazzani, R.-M., Roxburgh, I. W., & Dupret, M.-A. 2015, A&A , 579, A116

Pasek, M., Lignières, F., Georgeot, B., & Reese, D. R. 2012, A&A , 546, A11

Pesnell, W. D. 1990, ApJ , 363, 227

Poretti, E., Michel, E., Garrido, R., et al. 2009, A&A , 506, 85

Prat, V., Lignières, F., & Ballot, J. 2016, A&A , 587, A110

Reese, D., Lignières, F., & Rieutord, M. 2008, A&A , 481, 449

Reese, D. R., MacGregor, K. B., Jackson, S., Skumanich, A., & Metcalfe, T. S. 2009, A&A , 506, 189

Reese, D. R., Prat, V., Barban, C., van 't Veer-Menneret, C., & MacGregor, K. B. 2013, A&A , 550, A77

Roxburgh, I. W. 2006, A&A , 454, 883

Roxburgh, I. W., Griffith, J. S., & Sweet, P. A. 1965, Zeitschrift für Astrophysik, 61

Royer, F., Grenier, S., Baylac, M.-O., Gï¿œmez, A. E., & Zorec, J. 2002, Astronomy and Astrophysics, 393, 897

Sackmann, I.-J. & Anand, S. P. S. 1970, The Astrophysical Journal, 162, 105

Saio, H. 1981, ApJ , 244, 299

Saio, H. & Cox, J. P. 1980, ApJ , 236, 549

Scuflaire, R. 1974, A&A , 36, 107

Shajn, G. & Struve, O. 1929, Monthly Notices of the Royal Astronomical Society, 89, 222

Short, C. I., Hauschildt, P. H., & Baron, E. 1999, ApJ , 525, 375

Simon, R. 1969, A&A , 2, 390

Slettebak, A. 1949, ApJ , 110, 498

Slettebak, A., Kuzma, T. J., & Collins, G. W. 1980, ApJ , 242, 171

Soufi, F., Goupil, M. J., & Dziembowski, W. A. 1998, A&A , 334, 911

Struve, O. & Elvey, C. T. 1931, MNRAS , 91, 663

Suárez, J. C., García Hernández, A., Moya, A., et al. 2014, A&A , 563, A7

Suárez, J. C., Goupil, M. J., Reese, D. R., et al. 2010, ApJ , 721, 537

Suran, M. D. 2008, Ap&SS , 316, 163

Sweet, I. P. A. & Roy, A. E. 1953, MNRAS , 113, 701

Takata, M. & Saio, H. 2013, PASJ , 65, 68

Takeda, Y., Kawanomoto, S., & Ohishi, N. 2008, ApJ , 678, 446

Tassoul, M. 1980, ApJS , 43, 469

Templeton, M. R., McNamara, B. J., Guzik, J. A., et al. 1997, AJ , 114, 1592

Townsend, R. H. D. 2003, MNRAS , 340, 1020

van Belle, G. T., Ciardi, D. R., Thompson, R. R., Akeson, R. L., & Lada, E. A. 2001, ApJ , 559, 1155

von Zeipel, H. 1924, MNRAS , 84, 665

Walker, G., Matthews, J., Kuschnig, R., et al. 2003, PASP , 115, 1023

Walraven, T. & Walraven, J. H. 1960, Bull. Astron. Inst. Netherlands , 15, 67

Yoon, J., Peterson, D. M., Kurucz, R. L., & Zagarello, R. J. 2010, ApJ, 708, 71

Yoon, J., Peterson, D. M., Zagarello, R. J., Armstrong, J. T., & Pauls, T. 2008, ApJ, 681, 570

Yoshida, S. & Eriguchi, Y. 2001, MNRAS , 322, 389

Zhao, M., Monnier, J. D., Pedretti, E., et al. 2009, ApJ , 701, 209